Remote Sensing of Environment 323 (2025) 114724

Contents lists available at ScienceDirect

Remote Sensing of Environment

journal homepage: www.elsevier.com/locate/rse

Application of satellite and proximal hyperspectral sensing to target lithium mineralization in volcano-sedimentary deposits: A case study from the McDermitt caldera, USA

F. Corrado [a], F. Putzolu [b,*], R.N. Armstrong [b], N. Mondillo [a,b], R. Chirico [c], B. Casarotto [c], M. Massironi [c], D. Fuller [d], R. Ball [e], R.J. Herrington [b]

[a] Department of Earth, Environment and Resources Science, University of Naples Federico II, Naples, Italy
[b] Resourcing the Green Economy Theme, Natural History Museum, United Kingdom
[c] Department of Geosciences, University of Padua, Italy
[d] Image and Analysis Centre, Natural History Museum, United Kingdom
[e] Jindalee Lithium Ltd, Perth, Australia

ARTICLE INFO

Edited by: Jing M. Chen

Keywords:
lithium
McDermitt caldera
Mineral exploration
Hyperspectral analysis
EnMap

ABSTRACT

This study provides satellite and proximal hyperspectral analyses of lithium (Li)-bearing volcano-sedimentary environments aimed at determining the target absorption features of alteration assemblages to be used as exploration vectors towards analogous Li-mineralized systems.

The study was applied at the McDermitt caldera (USA), which hosts volcano-sedimentary Li mineralization in the form of clay minerals originated from the alteration of glass-rich extrusive igneous rocks in endorheic lacustrine basins. The surface-exposed areas of the caldera were investigated using satellite hyperspectral imagery acquired by the German Environmental Mapping and Analysis Program (EnMAP) mission. Satellite data were validated via ground spectroscopy, performed through hyperspectral imaging, complemented by mineralogical and geochemical analyses on specimens deriving from the Jindalee McDermitt Li deposit.

The Li mineralization in the Jindalee McDermitt deposit is dominated by a Mg(Li)-smectite (hectorite) + amorphous silica assemblage, showing absorption features at 2306 nm and 2200 nm that can be detected in the spectral range covered by the EnMAP sensor. The analysis of the corresponding hyperspectral feature distribution maps and the comparison with ground control samples, confirmed that the above features together can be effectively used as mineralogical-hyperspectral vectors for Li-prospective areas on a caldera-scale. This spectral footprint was used in the analysis of a similar system that lacks Li mineralization (High Rock caldera complex, USA). Results of this test show that the distinctive 2200 + 2306 nm bands association is lacking at the High Rock caldera complex, which suggests that this spectral footprint can be employed as a mappable criteria to target lacustrine sequences with mineralogical features analogous to those of Li-mineralized volcano-sedimentary deposits.

1. Introduction

The growing demand for lithium linked to the proliferation of low-emissions energy technologies requires the development of novel exploration tools to be applied for the effective targeting of new mineral deposits. As the research for new Li resources intensifies, unconventional ore types such as volcano-sedimentary Li deposits have become potential targets for mineral exploration in addition to pegmatite and brine systems (Bowell et al., 2020). Volcano-sedimentary deposits include Li mineralization in the form of clay minerals and/or borosilicates ore assemblages formed from the alteration of Li-fertile felsic igneous rocks deposited in shallow lacustrine settings (e.g., Putzolu et al., 2025).

In this context, hyperspectral analysis is a powerful tool for targeting these complex mineral associations since it can effectively detect and characterize hydrous phases and reveal their alteration patterns (Calvin and Pace, 2016; Cudahy et al., 2008; Sorrentino et al., 2024). Through its ability to detect subtle variations in mineral absorption features,

* Corresponding author.
E-mail address: francesco.putzolu1@nhm.ac.uk (F. Putzolu).

https://doi.org/10.1016/j.rse.2025.114724
Received 8 November 2024; Received in revised form 17 March 2025; Accepted 25 March 2025

hyperspectral sensing provides insights into the spatial distribution of minerals and alteration zones at both regional and local scales (Asadzadeh et al., 2024; Chabrillat et al., 2024). The increasing use of reflectance spectra data to generate mineralogical maps is being supported by advances in instrumentation, spectral libraries, and algorithms (e.g., Kokaly et al., 2017; Kumar et al., 2020; Thiele et al., 2021).

This has resulted in a much wider application of hyperspectral analysis to study igneous Li mineralization in pegmatite and granite systems. Specifically, hyperspectral methods have been successfully employed to target Li-mineralized magmatic-hydrothermal assemblages (i.e., spodumene and Li-micas) and their associated alteration halos based on satellite-born data (e.g., Cardoso-Fernandes et al., 2020; Jiang et al., 2023) and through proximal outcrop- to sample-scale hyperspectral mapping (Booysen et al., 2022; Kirsch et al., 2023). Application of hyperspectral methods to clay-rich Li deposits is limited to a scoping study on the spectral signature Li-smectites from the McDermitt caldera (Meyer et al., 2023). However, a systematic and integrated hyperspectral-mineralogical study of clay-rich volcano-sedimentary Li deposits that encompasses proximal- and satellite-based methods is still missing, therefore hampering the application of hyperspectral-based protocols to inform mineral exploration for this Li mineralization type. In the present work, we have investigated the volcano-sedimentary Li mineralization located in the McDermitt caldera (Nevada-Oregon, USA), by using satellite and proximal hyperspectral analyses. The McDermitt caldera is home to one of the world's largest lithium resources with an estimated ~20 to 40 Mt. of contained Li (Castor and Henry, 2020), and hosts significant Li deposits such as the Lithium Americas Thacker Pass (Nevada, USA) and the Jindalee McDermitt (Oregon, USA) deposits. Although the Thacker Pass and Jindalee McDermitt deposits lie within the same intra-caldera setting, they show distinct structural and stratigraphic configurations, influencing exploration strategies for adjacent lithium clay targets. The clay-rich orebody at the Thacker Pass deposit is located in a significantly collapsed area of the caldera and is largely covered by alluvium and lava flow units (Benson et al., 2017a, 2023), while lacustrine clays in the Jindalee McDermitt deposit, as well as in the rest of the northern sector of the caldera, are locally exposed and lack significant cover (Castor and Henry, 2020; Henry et al., 2017). Recent research has shown that the genesis of Li-clays in the Jindalee McDermitt Deposit was accompanied by extensive neoformation of aluminosilicates (i.e., zeolites and secondary feldspars) and by segregation of diagenetic silica (Putzolu et al., 2023), thus making these phases potential indicators for mapping poorly constrained mineralized areas in the McDermitt caldera and in other similar settings. This contribution is aimed at (1) establishing target absorption features of significant minerals or association of minerals related to volcano-sedimentary Li deposits; (2) mapping lithologies and alteration haloes at the satellite and sample scale by using selected target features; (3) defining alteration footprints/patterns and potential Li prospective zones within the McDermitt caldera; (4) defining potential mineralogical-hyperspectral vectors to be used for exploration of undiscovered volcano-sedimentary Li mineralization. The mineralogical-hyperspectral vectors established for the Li mineralization at McDermitt has been also applied to feed a test on the High Rock caldera complex (USA), which although shares similar geological features with

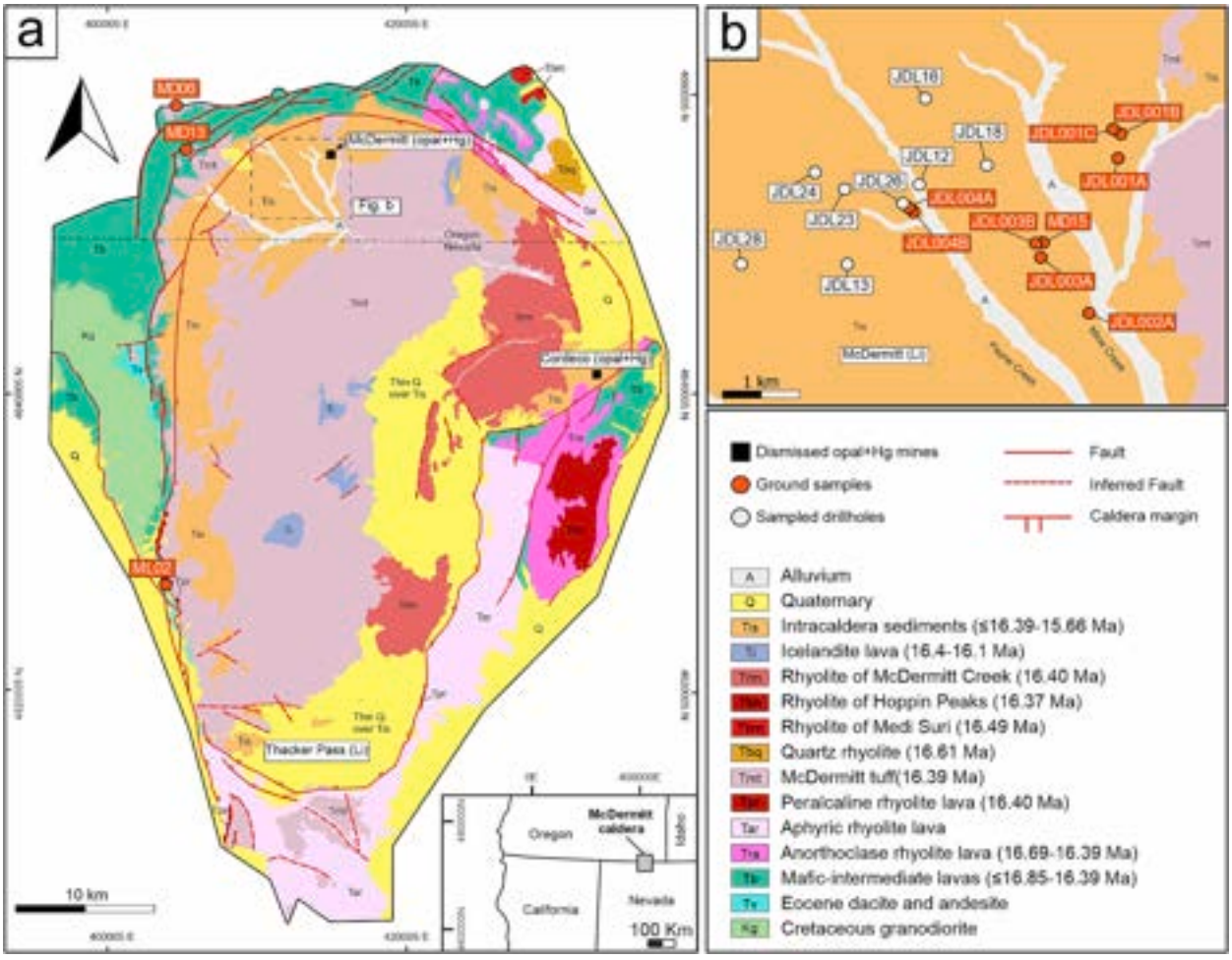

Fig. 1. a) Geological map of the McDermitt caldera (USA) showing the location of the Jindalee McDermitt and Lithium Americas Thacker Pass Li deposits (modified after Henry et al., 2017); b) close-up view on the Jindalee McDermitt tenure showing the distribution of the ground specimens and of the sampled drillholes.

the McDermitt caldera, is not mineralized.

2. Geology of the McDermitt caldera and associated volcano-sedimentary lithium mineralization

The McDermitt caldera (Fig. 1a), situated at the border between Nevada and Oregon (USA), is a large silicic volcanic center that originated during the initial development of the Yellowstone hotspot and Columbia River basalt volcanism (Benson et al., 2017b; Castor and Henry, 2020; Coble and Mahood, 2012; Henry et al., 2017). The caldera structure formed during the eruption of the 16.39 ± 0.02 Ma McDermitt tuff that released ~1000 cubic km^3 of igneous extrusive material, which included highly fractionated, peralkaline to metaluminous rhyolitic rocks with elevated pre-eruptive Li and F concentrations (Benson et al., 2017a; Henry et al., 2017 and references therein). The latest evolutionary stages of the system (until 16.08 ± 0.10 Ma) were dominated by intermediate volcanism leading to post-collapse resurgence and subsequent doming of the caldera structure (Castor and Henry, 2020; Henry et al., 2017).

The volcano-sedimentary Li mineralization is well exposed in the northern sector of the caldera (i.e., Jindalee McDermitt Li deposit), while other ores are locally covered by alluvium and/or lava flows in the southern (i.e., Thacker Pass Li deposit) and in the eastern sides of the system (Fig. 1a). Deposition of the volcano-sedimentary units occurred shortly after the caldera collapse and continued after the episode of doming, leading to the development of lacustrine sequences consisting of mixed extrusive igneous rocks (i.e., ash falls and proximal pyroclastics) and lithium claystones with a thickness of up to ~200 m (Castor and Henry, 2020; Henry et al., 2017). Previous studies have shown that the bulk of the Li mineralization on a caldera-scale is linked to the early diagenetic alteration of the extrusive rocks of the McDermitt tuff and subsequent formation of Li-rich Mg-smectite (hectorite) associated with other secondary aluminosilicates such as zeolites and feldspars (Benson et al., 2023; Castor and Henry, 2020; Putzolu et al., 2023). However, the southern part of the system (i.e., Thacker Pass Li deposit) records a distinctive mineralizing event possibly linked to circulation of higher temperature Li(F)-rich fluids that led to extensive breakdown of hectorite and subsequent Li-illite (tainiolite-like) formation at depth in the volcano-sedimentary sequence (Benson et al., 2023).

The Jindalee McDermitt Li deposit (Fig. 1b) occurs as sub-horizontal

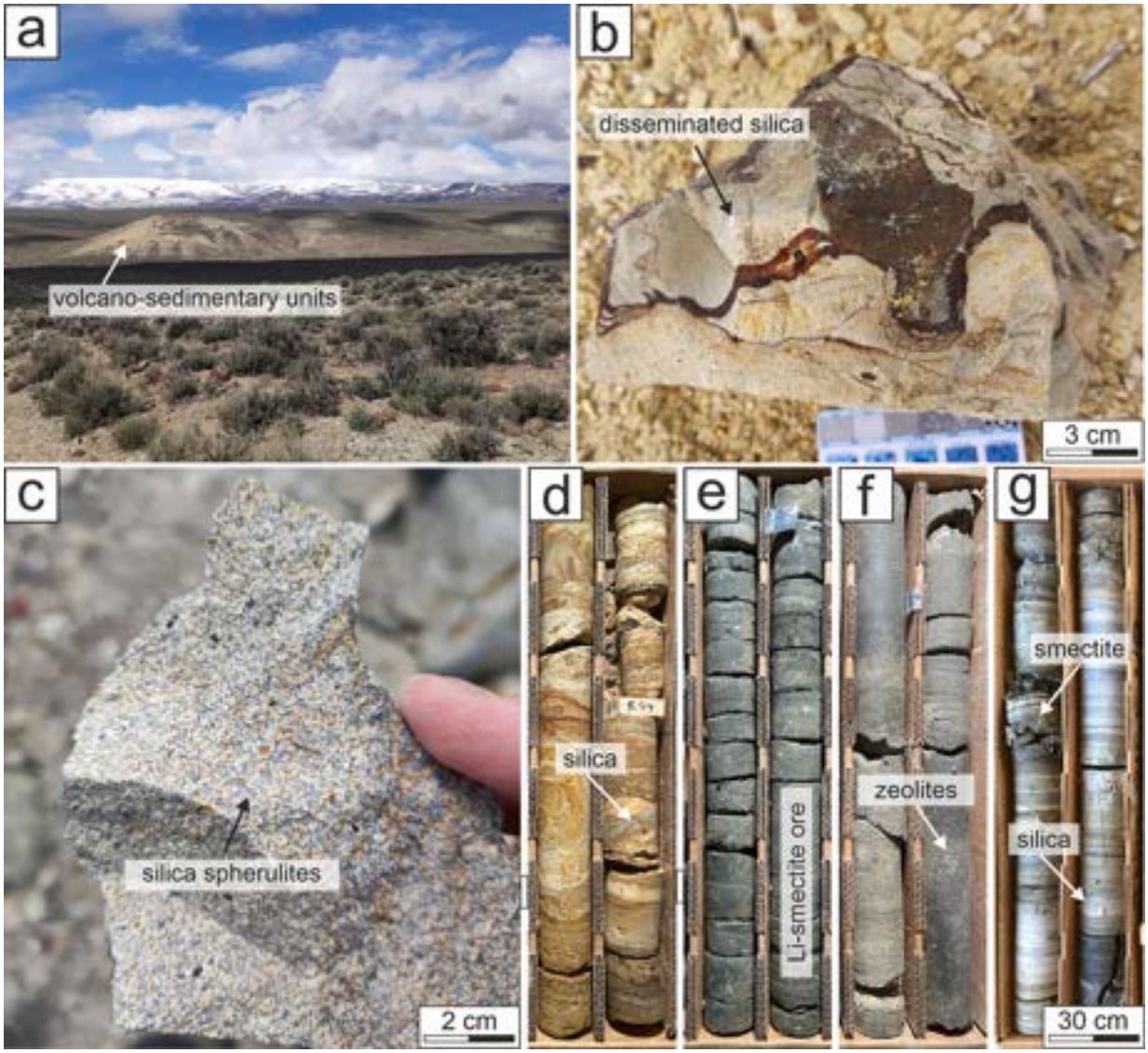

Fig. 2. Lithium mineralization in the Jindalee McDermitt deposit: a) outcropping volcano-sedimentary units; b) shallow silicified overburden unit; c) outcropping tuffaceous material with spherulitic silica alteration; d) silicified overburden unit at the top of the McDermitt orebody; e) lithium claystone; f) zeolitized intrabasinal unit; g) lacustrine sediments with silica-smectite intercalations.

stratiform sequence of volcano-sedimentary lithologies, which are largely exposed by incising creeks resulting in the formation pale colored escarpments with outcropping Li-rich smectites. (Fig. 2a). The orebody is partly covered by an overburden unit that occurs along the ridge lines forming between the incising creeks, and comprises silicified and oxidized tuffaceous material (Fig. 2b), which locally shows silica spherulitic textures resulting from the devitrification of volcanic glass material (Fig. 2c). The overburden unit is intercepted at depths of up to maximum 20 m within the deposit and shows silicification-oxidation features analogous to those observed at surface (Fig. 2d). The bulk of the orebody includes massive to bedded lithium claystones associated with carbonates (Fig. 2e), extrusive igneous rocks altered to nodular zeolites (Fig. 2f) and finely laminated siliceous sediments interlayered with altered volcanic ash and smectite (Fig. 2g).

3. Geology of the High Rock caldera complex

The High Rock caldera complex (Nevada, USA) is located approximately 40 km west to the McDermitt caldera (see Appendix A) and includes four major caldera structures (i.e., Virgin Valley, Badger Mountain, Hanging Rock and Cottonwood Creek calderas) that developed during several episodes of eruption of large volumes of rhyolitic to trachytic magmas (Coble and Mahood, 2016). The magmatic history of the High Rock caldera complex lasted between 16.5 and 15.5 Ma, and was marked by the emplacement of highly fractionated extrusive rocks with ages and compositions similar to those observed in the nearby McDermitt caldera (Coble and Mahood, 2016; Henry et al., 2017). The igneous suite at the High Rock caldera complex includes peralkaline to alkaline effusive and extrusive units with a rhyolitic composition, which are chronologically bracketed by metaluminous rhyolites, while more intermediate and mafic effusive lithologies are volumetrically subordinate. The caldera-forming eruptions at the High Rock caldera complex resulted in multiple episodes of volcanic subsidence and formation of intracaldera fill deposits, which, as opposed to the McDermitt caldera, largely comprise preserved subaerial extrusive units (Coble and Mahood, 2016). Episodes of lacustrine sedimentation at the High Rock caldera complex were disrupted by abrupt changes in the caldera topography linked to catastrophic volcanic events, which likely prevented the formation of volcano-sedimentary Li mineralization. Lacustrine sediments are mostly observed in the areas of greater volcanic subsidence within the Virgin Valley and Hanging Rock calderas where alteration of rhyolite units lead to the local formation of diagenetic assemblages (Castor and Henry, 2000), yet no economic volcano-sedimentary Li mineralization have been documented so far.

4. Materials and methods

4.1. Analytical workflow and sampling strategy

The analytical workflow adopted for this study involved several stages aimed at identifying mappable minerals associated with the volcano-sedimentary Li mineralization of the McDermitt caldera (Fig. 3). The first step of the workflow involved the selection of target minerals found in samples representative of the Li mineralization established using conventional mineralogical and geochemical analyses, such as X-ray diffraction (XRD), scanning electron microscopy and energy-dispersive X-ray spectroscopy (SEM-EDS), automated-SEM, Fourier-transform infrared spectroscopy (FTIR), electron probe microanalysis (EPMA) and bulk-rock geochemistry. Details of the analytical procedures are reported in Appendix B. Once the key mineral targets were established, hyperspectral data were acquired from representative ground samples to determine target absorption features associated with significant mineral phases that could be mapped utilizing satellite-based data. Reflectance spectra and hyperspectral images of ground samples were acquired using the Headwall Photonics Nano- and Micro-Hyperspectral cameras housed at the Department of Geosciences of the University of Padua (Italy). These laboratory analyses were performed on 48 samples collected from drillholes and outcrops located in the Jindalee McDermitt tenure, as well as in other areas of the caldera (see Appendix C). Within the considered sample suite, 12 specimens were collected from the shallow units at the top of the orebody in the Jindalee McDermitt tenure and from the volcanic country rocks in order to study the hyperspectral footprint of the outcropping lithologies. The remaining samples represent the key facies identified in the Li orebody, including lithium claystones, zeolitized igneous rocks and siliceous lacustrine sediments. Subsequently, EnMAP scenes were acquired to investigate the exposed outcrops within the study area, further extending the spatial resolution of the study to a broader regional scale.

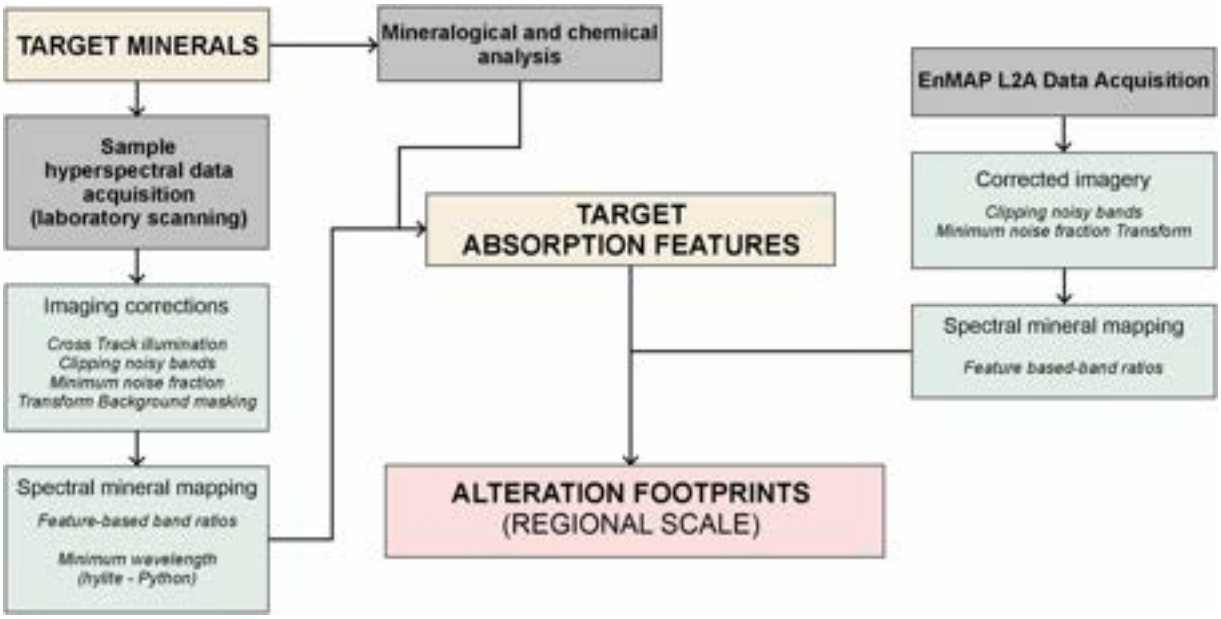

Fig. 3. Schematic workflow showing the pre-processing and processing steps used in this study.

4.2. Current knowledge on short-wave infrared (SWIR) features of target minerals

Based on previous work on the Jindalee McDermitt Li deposit (Putzolu et al., 2023), potential target minerals for the study area include smectite clays, carbonates, amorphous silica and zeolites.

Within the smectite group, the main absorption features arise from octahedral cations associated with hydroxyl groups, leading to specific vibrational responses of Al-OH, Fe-OH, and Mg-OH bonds. Aluminum-bearing smectites (e.g., montmorillonite) display a strong absorption feature at approximately 2200 nm, attributed to the combination of ν and δ Al_2OH vibrations. Intense absorption features are also observed at 1410 nm and 1910 nm, respectively associated with $2\nu OH$ and with the water absorption (Clark et al., 1990). Substitution of octahedral Al^{3+} by divalent cations such as Fe^{2+} or Mg^{+2} leads to a charge imbalance compensated through tetrahedral Al^{3+} replacement by Si^{4+}, resulting in a shift of absorption features to longer wavelengths as the amount of Al^{3+} replaced by divalent cations increases (Bishop et al., 2008; Laukamp et al., 2021). The diagnostic features of Fe-smectites (e.g., nontronite) are detected near 2290 nm ($\nu + \delta$ Fe^{3+} 2OH), as well as 1410 nm, 1430 nm, and 1910 nm. Chemical variations within the group can be attributed at the presence of $AlFe^{3+}$-(or Mg) and $Fe^{3+}Fe^{3+}$-OH, which cause shifts in the absorption centers from shorter to longer wavelengths, respectively (Bishop et al., 2008).

Hectorite, a Mg(Li)-smectite, shows two major absorption features near 1910 nm and 1410 nm, each having a shoulder near 1450 nm and 1960 nm. The diagnostic absorption is centered at around 2306 nm, resulting from a combination of OH stretching and Mg-OH bending vibrations, with a minor additional feature, detected near 2386 nm (Kokaly et al., 2017). It is worth noting that the presence of Li in hectorite has no effect in producing distinctive absorption features in the investigated spectral range. Minerals sharing similar octahedral compositions, such as smectite and mica, exhibit comparable spectral responses; however, a notable shift towards longer wavelengths (~2220 nm) is observed in illite (Laukamp et al., 2021). Illite displays significant absorption bands at 1400 nm, 1900 nm, and 2200 nm, with 2340 nm and 2450 nm (Al-OH) used as diagnostic indicators to differentiate between micas and smectites (Clark et al., 1990; Meyer et al., 2022).

Amorphous silica (opal-like) presents a spectral response at 2200 nm accompanied by large and sharp features near 1416 nm and 1910 nm, which are produced by a combination of free OH stretching and siloxane (Si-O-Si) bending (Calvin and Pace, 2016; Chauviré et al., 2021; Goryniuk et al., 2004). Additionally, a minor and broad feature may occur around 1810 nm. The variability in the spectra of amorphous silica may result from differences in water content and how H_2O is bound to SiO_2 molecules.

In the 1000–2500 nm spectral range, zeolites exhibit a weak absorption feature at 1160 nm, related to a combination of a symmetric and asymmetric O-H stretching and H-O-H bending fundamental (Cloutis et al., 2002; Kodikara et al., 2023). A strong absorption feature occurs near 1400 nm, resulting from the H_2O stretching combined with the first overtone of the H_2O bending. Furthermore, relatively weak absorption features are observed in the 1780 nm and 1900 nm regions (Cloutis et al., 2002).

The diagnostic asymmetric absorption features of carbonates are found between 2300 nm and 2340 nm, which are associated with the $3\nu_3CO_3$ vibrational mode, primarily influenced by the substitution of Ca with Mg, Fe, and Mn in the carbonate structure (Gaffey, 1986; Laukamp et al., 2021). As Mg and Fe concentrations increase, the $3\nu_3CO_3$ feature shifts to shorter wavelengths (Gaffey, 1986). Calcite, in particular, exhibits a major absorption feature between 2336 nm and 2340 nm, while dolomite shows a shorter absorption feature around 2320 nm. Both carbonates also present medium to minor features at 1800 nm and 1900 nm (Laukamp et al., 2021).

4.3. Hyperspectral analysis of ground samples

The laboratory scanning process involved the acquisition of hyperspectral data and images from the surface of previously cut and planar-rendered samples. The hyperspectral images provide a representation of the surface of the samples in the VNIR (400–1000 nm) to SWIR (900–2500 nm) ranges. The VNIR acquisition has a spectral sampling distributed across 270 bands, while the SWIR acquisitions include 166 bands. The spatial resolution of the images varied depending on the laboratory acquisition conditions. For VNIR imaging, the spatial resolution was approximately 120 μm/pixel, achieved with a camera lens-sample distance of 29 cm, while the SWIR imaging was conducted with a spatial resolution of 220 μm/pixel and with a camera lens-sample distance of 25 cm. The resultant datacubes were analyzed through a series of pre-processing and processing steps to enhance data quality and to reduce the noise, using a set of tools available in ENVI 5.6 software and the open-source Python package “hylite” (Thiele et al., 2021). The pre-processing steps included imaging corrections to ensure the accuracy and reliability of spectral data. These corrections comprised (1) the cross-track illumination correction, applied to each datacube via a sample-based approach; (2) the removal of SWIR bands between 900 nm and 961 nm; and (3) the Minimum Noise Fraction (MNF) transform. The MNF transform (Green et al., 1988), reduces noise and dimensionality of hyperspectral data, allowing the detection of weak spectral features that can be critical for the identification and mapping of mineral targets. Four our dataset, the top components accounting for the majority of the spectral information were preserved, as determined by analysing the eigenvalues of the MNF components. The exact number of bands retained depended on the specific dataset. In our case, a selection of eight to ten components was employed, as they were identified as the primary contributors to the variability in the data, improving the signal-to-noise ratio, particularly in the bands containing relevant spectral information. Ultimately, the background was filtered using Region Of Interest (ROI)-based masks.

The spectral characterization and subsequent mapping of minerals within the samples were based on the diagnostic spectral responses of the mineral bond. The analytical techniques employed a combination of feature-based band ratio analysis and minimum wavelength mapping (Cudahy et al., 2008; Laukamp, 2022) to classify and map the mineral phases. The feature band ratio, focused on spectral parameters after continuum-removal, such as absorption band depth and absorption wavelength position of absorption features associated with target minerals. These spectral parameters offer key information regarding the presence and abundance of mineral phases. Specifically, the depth of an absorption band is indicative of the relative abundance of vibrational bonds associated with the target minerals, while the position of the absorption feature can be linked to their chemical composition (Clark et al., 1990; Cudahy et al., 2008; Laukamp et al., 2021). The minimum wavelength mapping technique is used to identify the wavelength positions of the deepest absorption features within spectral images. This method combines both position and depth information of the deepest absorption features, generating a detailed per-pixel overview map of the predominant bond occurrences. These maps provide visual information about the mineral distribution across the surface of the sample, as they highlight areas of high mineral concentration and offer insights into their chemical composition. Furthermore, such maps are complemented by corresponding spectra, which offer a characterization of the occurring minerals, including their spectral signatures and chemical compositions. For the mineral phases of interest, the analysis was focused on the SWIR wavelength range between 2120 nm and 2400 nm.

As part of the hyperspectral data processing chain, band ratios were used to identify amorphous silica, zeolite, and calcite. Conversely, the minimum wavelength method was applied to distinguish zeolite, hectorite, and Fe-smectite. To estimate the relative abundance of amorphous silica, the absorption feature at 2200 nm was analyzed using the band ratio $(R_{2168} + R_{2235})/R_{2206}$, referred to as the 2200 index, where R_λ

represents the reflectance at wavelength λ. To capture silica phases with variable chemical composition, the minimum wavelength mapping was performed to map the position of the 2200 nm absorption feature using a quadratic fitting approach (adapted from Thiele et al., 2021), which allowed for interpolating the absorption depth after the continuum removal within the 2180 and 2235 nm range. Relative abundance of zeolites was obtained using the 1800D index, derived from the ratio $(R_{1736} + R_{1823})/R_{1794}$, and mapping the 1161 nm feature with the minimum wavelength method (continuum removal between 1133 and 1181 nm). Calcite was identified based on the presence of CO_3 using the ratio $(R_{2311} + R_{2359})/R_{2340}$ (2340D index). The spatial distributions of hectorite and Fe-smectites were mapped using the minimum wavelength method following the continuum removal between 2283 and 2321 nm and between 2273 and 2302 nm, respectively.

4.4. Satellite hyperspectral data collection and processing

The hyperspectral EnMAP scenes covering the McDermitt caldera (2 images in total) were acquired on 22 June 2024 (UTC), whereas the hyperspectral EnMAP scenes covering the High Rock caldera complex (2 images in total) were acquired on 23 September 2024 (UTC). The images were obtained from the EOWEB GeoPortal https://eoweb.dlr.de/egp/ managed by the German Aerospace Center (2022). EnMAP operates as a pushbroom hyperspectral imager, designed to capture spectral data across a broad range of wavelengths. The instrument provides a broad spectral range spanning from 420 nm to 1000 nm (VNIR) and from 900 nm to 2450 nm (SWIR). EnMAP is characterized by high radiometric resolution and stability across both VNIR and SWIR spectral domains. The instrument provides a swath width of 30 km, achieving a spatial resolution of 30 × 30 m, with a nadir revisit time of 27 days and an off-nadir capability of up to 30°, which enhances its flexibility in capturing data from different angles and increasing coverage efficiency in areas of interest (Chabrillat et al., 2024).

The data used for this study were the Level 2-A (L2A) land products, already corrected using the L2A land processor based on the PACO (Python-based Atmospheric Correction) library (de Los Reyes et al., 2020). The L2A data were analyzed by pre-processing and processing steps. The pre-processing was aimed at reducing noise and improving the interpretability of the hyperspectral data. First, spectral regions with low signal-to-noise ratios or affected by instrument limitation were identified and eliminated assuring that only data of the highest quality would be subjected to analysis. The Minimum Noise Fraction (MNF) transform was also applied to the dataset, as explained in the previous section.

The spectral mineral mapping was performed by applying selected diagnostic band ratios of target minerals. These ratios were used for extracting the relative intensity of the absorption feature and to target the alteration footprint at the caldera-scale. Specifically, the ratios $(R_{2165} + R_{2232})/(R_{2207})$ and $(R_{2265} + R_{2373})/(R_{2306})$ were employed to highlight areas with high occurrences of the 2200 nm and 2306 nm features, respectively. Considering the mathematics of these formulas, a band ratio value equal to 2 is associated with the absence of absorption feature in the spectrum. In our dataset, the $(R_{2265} + R_{2373})/(R_{2306})$ ratio is always higher than 2, whereas the $(R_{2165} + R_{2232})/(R_{2207})$ ratio is locally also lower than 2 in association with spectra characterized by very broad absorption around 2100 nm, and varies continuously until a maximum value of 2.17. To assess the significance of the obtained band ratios, a minimum threshold was determined using a robust statistical approach. Plotting in a histogram the band ratio values corresponding to the pixels in the scene, it appears that the data have a bell-shaped distribution with a positively skewed tail. The threshold values were identified by analysing the second derivative of the curve that best represents the dataset. Specifically, the data distribution was interpolated using a univariate spline function, and the second derivative was computed to locate the point of maximum curvature. The point of maximum curvature, corresponding to the peak value of the second derivative, was considered the optimal threshold for distinguishing the significant spectral features. For the 2200 nm absorption features, the threshold was calculated to be approximately 2.03, based on this combined statistical and mathematical analysis.

The diagnostic band ratios of target minerals detected at the McDermitt site, were also used to feed the test carried out on the High Rock Caldera Complex (Nevada, USA).

5. Results

5.1. Geochemical and hyperspectral-mineralogical analyses of ground and drillhole samples

The selection of ground and drillhole samples for hyperspectral analysis was conducted to cover the lithostratigraphic facies identified in the McDermitt Li deposit by Putzolu et al. (2023). These include an overburden unit, which locally covers the Li mineralization, as well as a series of volcano-sedimentary units identified within the McDermitt orebody. The latter comprise the following facies: 1) lithium claystones; 2) zeolitized igneous rocks; and 3) siliceous lacustrine sediments. Bulk-rock geochemistry (Fig. 4a and Appendix C) has confirmed that the lithium claystone units are the main host for the mineralization. This unit displays Li grades (up to 3140 ppm) that are correlated with the Mg concentrations, supportive that hectorite is the main ore repository. More sporadic high Li concentrations are observed in the other volcano-sedimentary units, with maximum concentrations (up to 1675 ppm Li) measured in the siliceous lacustrine sediments. Anomalous Li concentrations (up to 1108 ppm Li) occur in the shallow lithologies occurring at the top of the orebody. Interestingly, also in this case the Li abundances are correlated with Mg, and follow the ideal stoichiometric line of hectorite (Fig. 4b), confirming that Li-bearing Mg-smectites are locally exposed at surface.

In the following subsections we present the hyperspectral-mineral maps and corresponding spectra of representative specimens of the selected lithostratigraphic facies. To validate the robustness of sample hyperspectral imaging, spatially resolved mineralogical and textural data (SEM-EDS, automated-SEM, FTIR and EPMA) are also provided.

5.1.1. Overburden

The more cohesive portion of the overburden units include extensively silicified lithologies that locally contain relict primary magmatic phases such as amphibole (Fig. 5a). In the hyperspectral analysis the presence of silica was associated with the bands at 2206 nm and 2215 nm (Figs. 5b-d). Furthermore, the detection of the Fe-OH bond feature at 2292 nm, associated with weak absorption around 1000 nm, supports the presence of oxidized Fe within late smectite veinlets (Figs. 5b-d).

5.1.2. Lithium claystones

Lithium claystones, representing the main Li ore, comprise hectorite, K-feldspar, zeolites, calcite and fine-grained silica (Figs. 6a, b). Hyperspectral imagery identified areas with elevated concentrations of hectorite and amorphous silica via the detection of the Mg-OH bond centred at 2302 nm, and the OH + O-Si-O bond of the silica at 2196 nm (Figs. 6c-e). Other relevant features of the lithium claystones include areas where hectorite is associated with calcite, showing the typical spectral response at 2330 nm ($3\nu_3CO_3$ band), and with zeolites, which were identified via the detection of the 1161 nm and ~1800 nm features (Figs. 6f-h).

5.1.3. Zeolitized igneous rocks

Igneous extrusive rocks from the McDermitt orebody show an alteration assemblage dominated by Na-zeolites, which according to mineralogical and textural analyses include analcime embedded in an amorphous silica groundmass (Fig. 7a). Spectral analysis identified regions dominated by analcime through the detection of the absorption features at 1161 nm and 1800 nm, indicative of the presence of OH

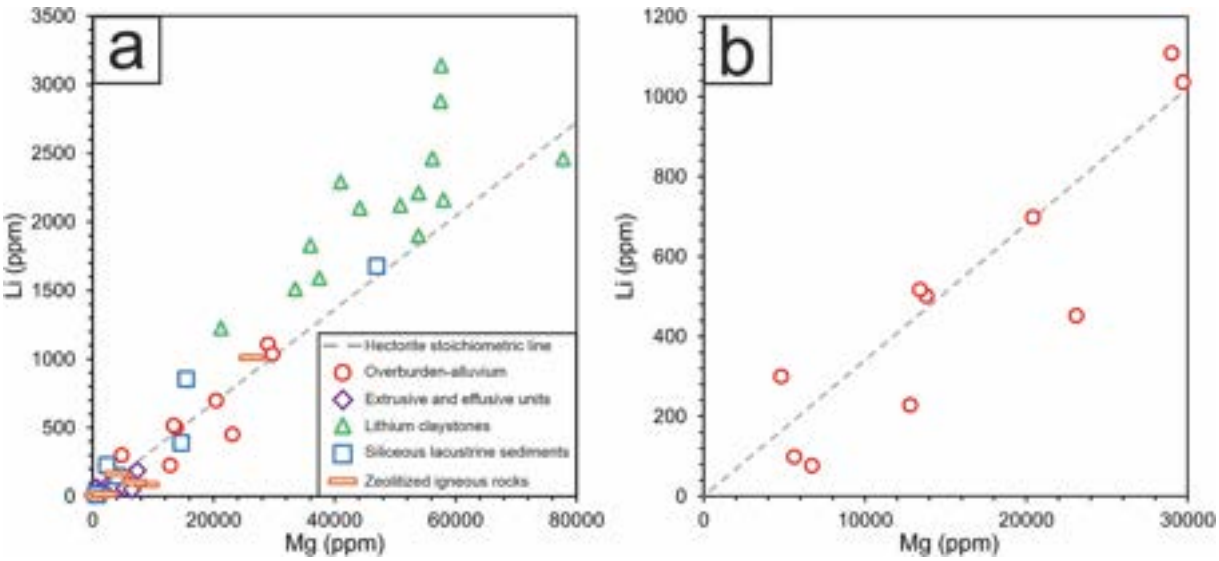

Fig. 4. a) Li (ppm) vs Mg (ppm) binary plot showing the Li-Mg positive correlation and the good match between the compositions of Li-bearing samples and the hectorite stoichiometric line (see Appendix C for geochemical dataset); b) enlargement of Fig. 4a. Note that the compositional line of hectorite has been calculated based on its nominal stoichiometric composition sourced from handbookofmineralogy.org.

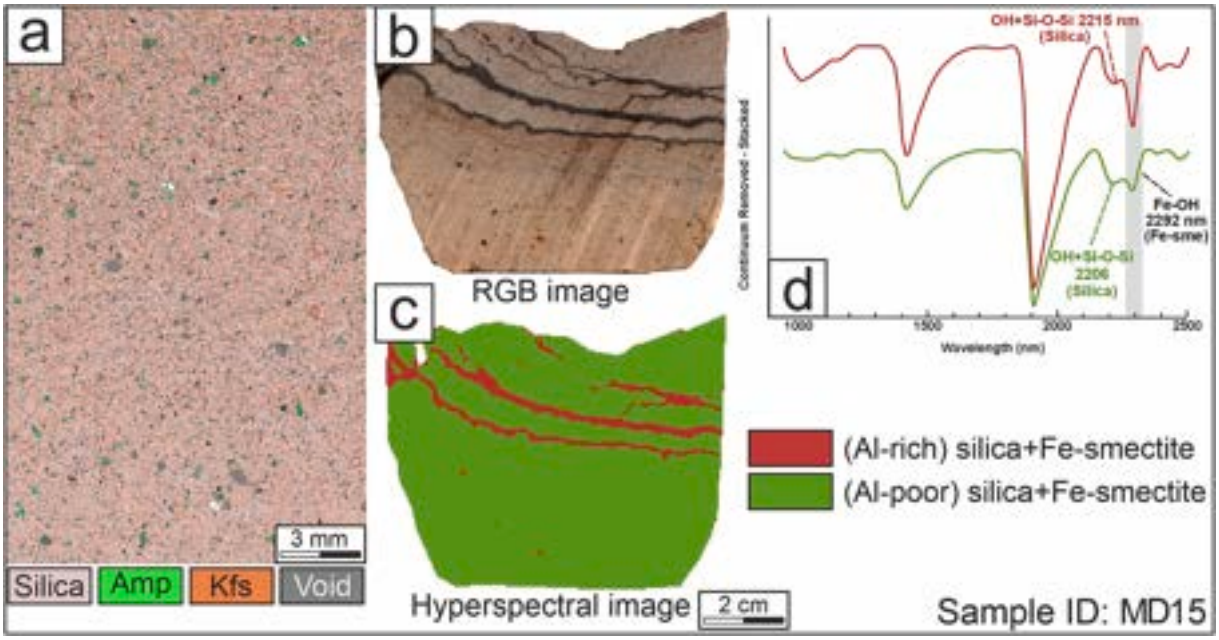

Fig. 5. Mineralogical and hyperspectral features of the overburden unit: a) automated-SEM mineral maps; b) and c) RGB and hyperspectral images of hand sample; d) spectral signatures of the main textural elements recognized in the hand sample. Sample type: ground. Abbreviations: Amp = amphibole; Kfs = K-feldspar; RGB = red-green-blue; SEM = scanning electron microscopy; Sme = smectite. (For interpretation of the references to colour in this figure legend, the reader is referred to the web version of this article.)

group within zeolites, while similarly to other facies the silica groundmass is associated with the 2215 nm band (Fig. 7b-d). Moreover, mineralogical analyses have shown that some zeolite-dominated samples comprise a Fe-smectite fraction (Fig. 7e), which upon hyperspectral imaging can be identified through the absorption features at 2283 nm and 2292 nm (Fig. 7f-h).

5.1.4. Siliceous lacustrine sediments

Mineralogical analyses indicate that siliceous lacustrine sediments are largely dominated by silica, with minor zeolites, K-feldspars and hectorite. Although in most instances these occur as laminated sediments, this facies locally show globular to spherulitic silica textures derived by the in-situ alteration of ash layers (Fig. 8; Putzolu et al., 2023). Hyperspectral analysis detected the distinctive features of the Mg-OH of hectorite (2302 nm) and of the OH + O-Si-O bond of the silica at 2196 nm, producing a mineral distribution map that matches well with the spatially resolved mineralogical characterization (Fig. 8).

5.2. FTIR and EPMA characterization of silica compounds

As shown by hyperspectral imaging, Li-mineralized specimens are characterized by secondary absorption features around 2200 nm, which can be attributed to hydration of silica compounds (Calvin and Pace, 2016; Chauviré et al., 2021; Goryniuk et al., 2004) that are closely

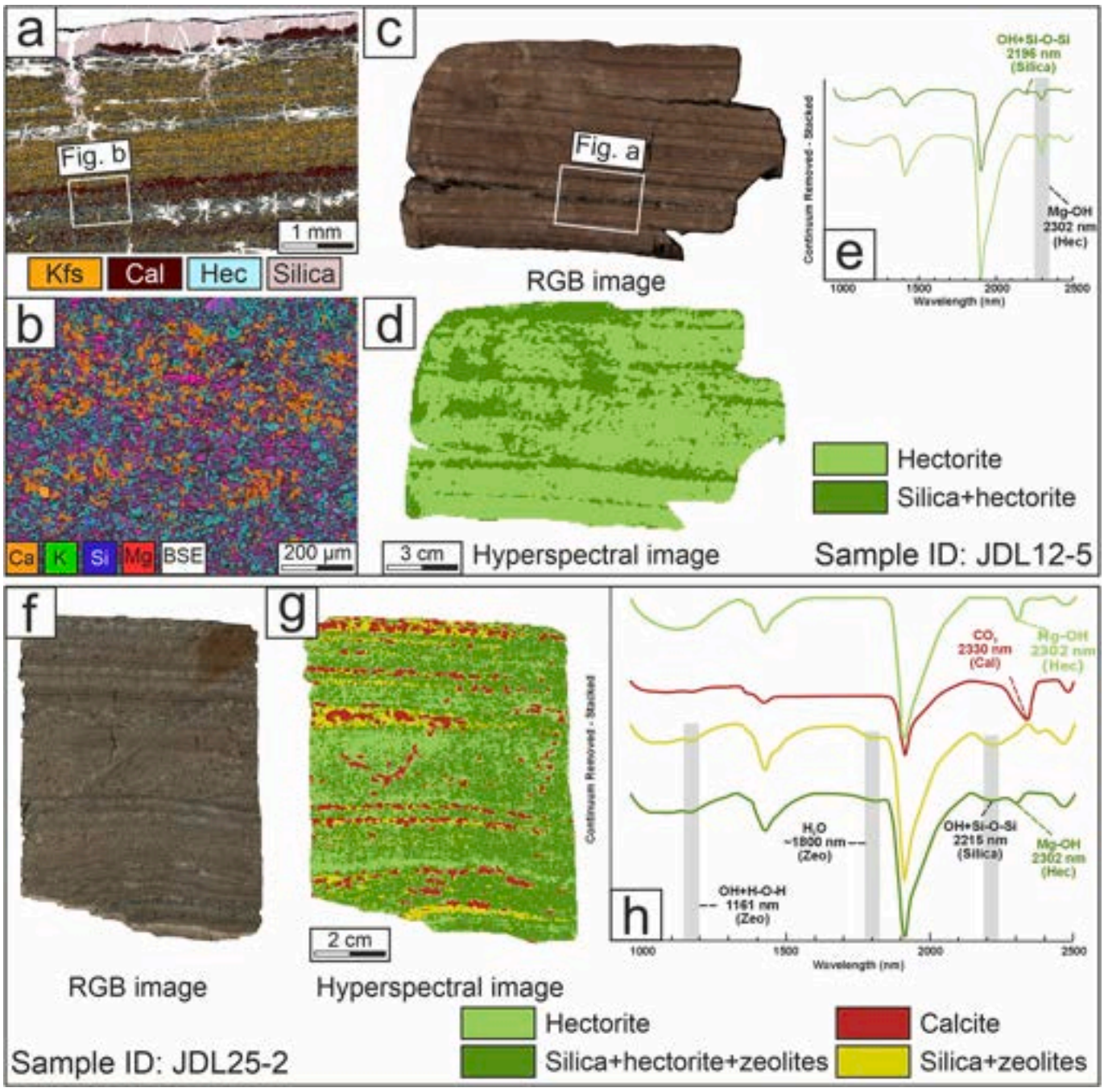

Fig. 6. Mineralogical and hyperspectral features of the lithium claystone unit: a) automated-SEM mineral map and BSE-EDS chemical map; c) and f) RGB images of hand samples; d) and g) hyperspectral images of hand samples; e) and h) spectral signatures of the main textural elements recognized in the hand samples. Samples type: drillhole. Abbreviations: BSE-EDS = backscatter electron and energy-dispersive X-ray spectroscopy; Cal = calcite; Hec = hectorite; Kfs = K-feldspar; RGB = red-green-blue; SEM = scanning electron microscopy; Zeo = zeolite. (For interpretation of the references to colour in this figure legend, the reader is referred to the web version of this article.)

associated with hectorite. To assess the water content and the nature of silica compounds we have carried out spatially resolved FTIR and EPMA analyses. The FTIR signature of the silica compounds is dominated by spectral bands at 1150 and 790 cm^{-1}, resulting from the stretching vibration of the Si-O-Si and Si-O bonds, and by a broad feature at around 3500 cm^{-1} that is due to structurally bonded H_2O and/or OH^- (Fig. 9). This spectral configuration supports that the amorphous silica is analogous to opal-A (Adamo et al., 2010). Electron probe microanalysis of silica compounds (see Appendix C) confirmed fluctuations in mineral chemistries linked to variable hydration degrees. Hydrous silica ($n = 50$) has water contents between 2300 and 5500 ppm H_2O and is characterized by significant concentrations of elemental impurities such as Al_2O_3, Fe_2O, K_2O and Na_2O, which respectively range between 0.62 and 4.66 wt%, 0.61–1.79 wt%, 0.01–4.12 wt% and 0.04–0.24 wt%. Quartz-like silica ($n = 27$) has water contents between 44 and 600 ppm H_2O and contains Al traces as main elemental impurity (Al_2O_3 between 0.19 and 0.64 wt%).

5.3. Hyperspectral satellite maps

The McDermitt caldera was investigated by interpreting EnMAP data, with a particular focus on the analysis of features at 2306 nm and

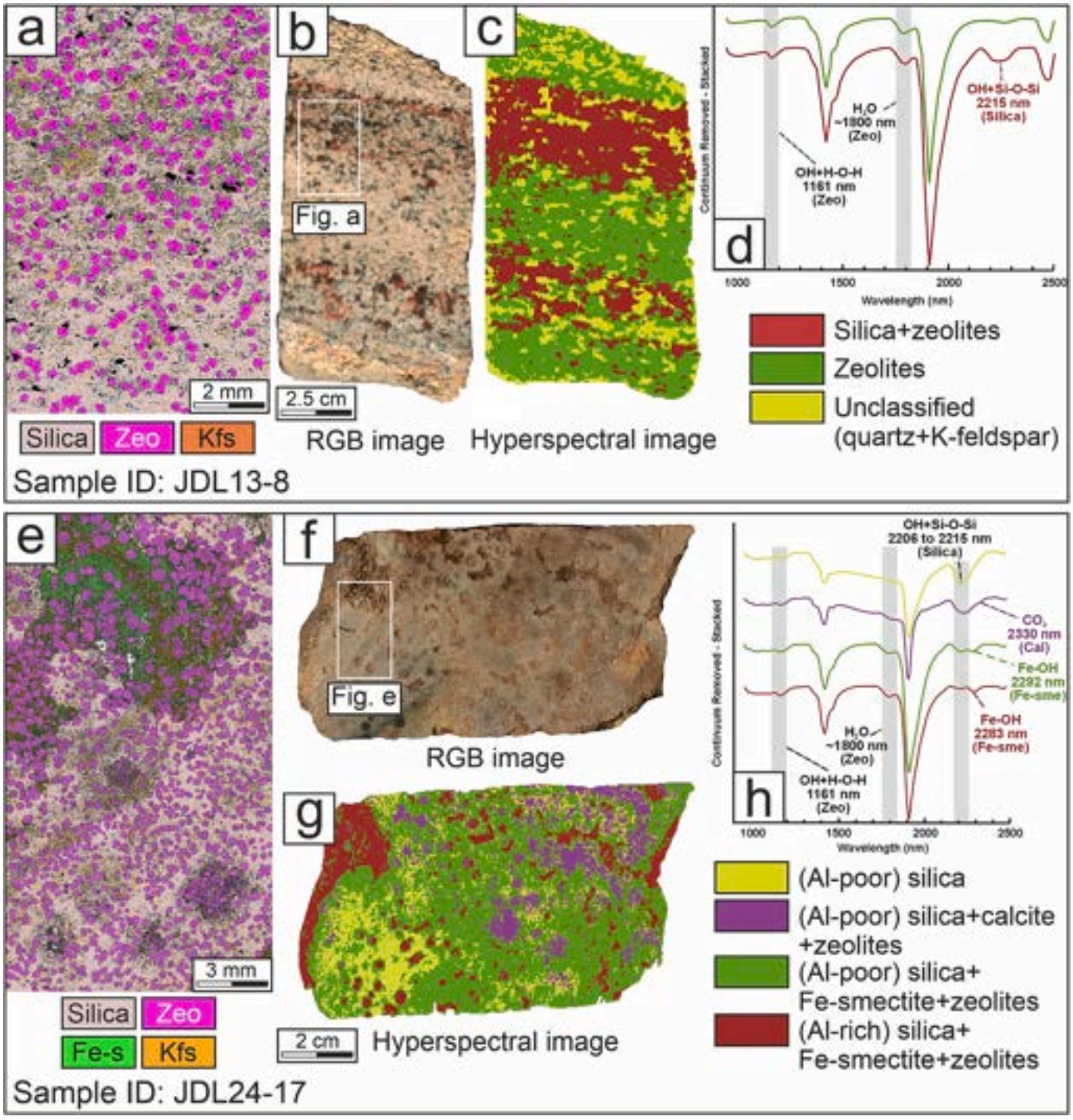

Fig. 7. Mineralogical and hyperspectral features of the zeolitized igneous units: a) and e) automated-SEM mineral map; b) and f) RGB images of hand samples; c) and g) hyperspectral images of hand samples; d) and h) spectral signatures of the main textural elements recognized in the hand samples. Samples type: drillhole. Abbreviations: Kfs = K-feldspar; Fe-s = Fe-smectite; RGB = red-green-blue; Sme = smectite; SEM = scanning electron microscopy; Zeo = zeolite. (For interpretation of the references to colour in this figure legend, the reader is referred to the web version of this article.)

2200 nm, which are dominant in the ore-bearing assemblage comprising hectorite and amorphous silica, and in the shallow units. The resulting maps delineate areas within the McDermitt caldera where these spectral features are particularly prevalent, as evidenced by their response in the electromagnetic spectrum recorded by the satellite platform.

The hyperspectral satellite map of the 2200 nm feature in the McDermitt caldera displays a significant relative abundance in the volcano-sedimentary units (Fig. 10a). The 2200 nm feature is particularly dominant in the NNW sector of the caldera, coinciding with the shallow lithologies outcropping in Jindalee McDermitt deposit (Fig. 10b). Other relevant areas where the 2200 nm feature shows high abundance are the eastern sector of the caldera, close to the dismissed Cordero opal mine (Fig. 10c), as well as in the southern sector in association with the dump material produced by the open pit workings of the Thacker Pass Li deposit (Fig. 10d). It is worth noting that the relevant absorption values of the 2200 nm feature in the open pit of the Cordero mine cannot be assessed because the EnMAP data do not cover that specific area. The distribution of the 2306 nm feature, corresponding to

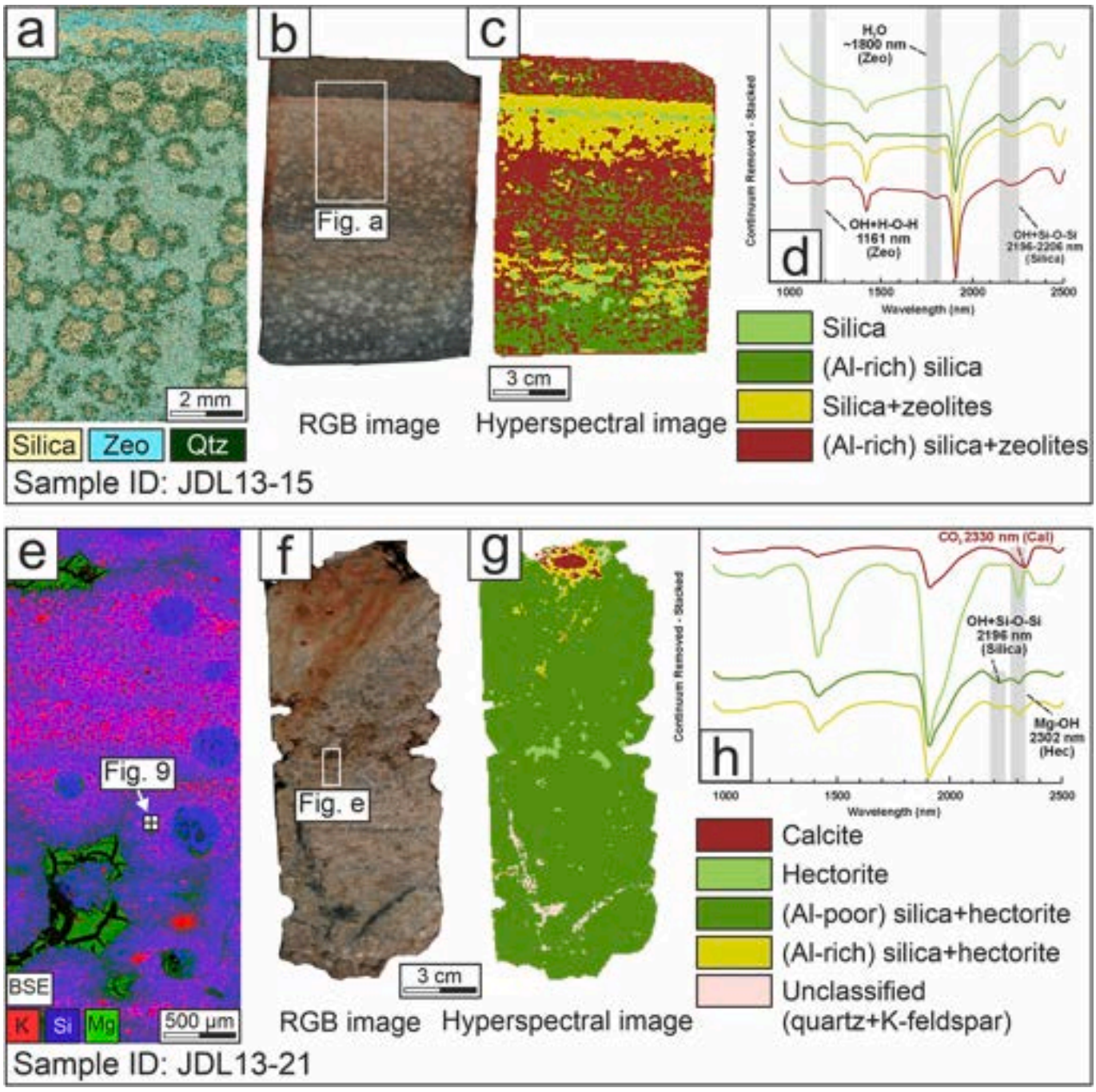

Fig. 8. Mineralogical and hyperspectral features of the siliceous lacustrine sediments: a) and e) automated-SEM and BSE-EDS maps of hand samples; b) and f) RGB images of hand samples; c) and g) hyperspectral images of hand samples; d) and h) spectral signatures of the main textural elements recognized in the hand samples. Samples type: drillhole. Abbreviations: BSE-EDS = backscatter electron and energy-dispersive X-ray spectroscopy; Hec = hectorite; Qtz = quartz; RGB = red-green-blue; Zeo = zeolite. (For interpretation of the references to colour in this figure legend, the reader is referred to the web version of this article.)

the Mg-OH bond, shows high values along the western sector of the caldera, where the outcropping units include barren igneous rocks (i.e., McDermitt tuff and pre-Miocene volcano-plutonic suite) and reworked sediments within the rivers and the drainage pattern (Fig. 11a-d). However, considering the relationship between the band ratio values of the 2200 nm and of the 2306 nm absorption features obtained from the two distinct maps (Fig. 12a), it can be observed that only a small set of data show the coexistence of both the 2200 nm and the 2306 nm band values above the threshold value of 2.03 (2306 nm band ratios between 2 and 2.045). When mapped, these data correspond to Li-prospective volcano-sedimentary units (Fig. 12b-c; Fig. 13). The coexistence of the features at 2200 nm and 2306 nm is well visible also in the McDermitt Li deposit area and in the sites selected for collection of ground control samples. Specifically, these locations exhibit pronounced absorption features at 2200 nm and 2306 nm (Appendix D) and show overall spectral footprints comparable to those detected through proximal hyperspectral analysis of the overburden units (Fig. 5). Lower 2306 band ratios comprised between 2 and 2.03, coexisting with maximum 2200 band ratios are mapped in the Thacker Pass area (Figs. 12a-c). Igneous units and the stream sediments have band ratios of the 2306 nm feature above the value of 2.045 and are not associated with 2200 values above the minimum significance threshold (Figs. 12a-c).

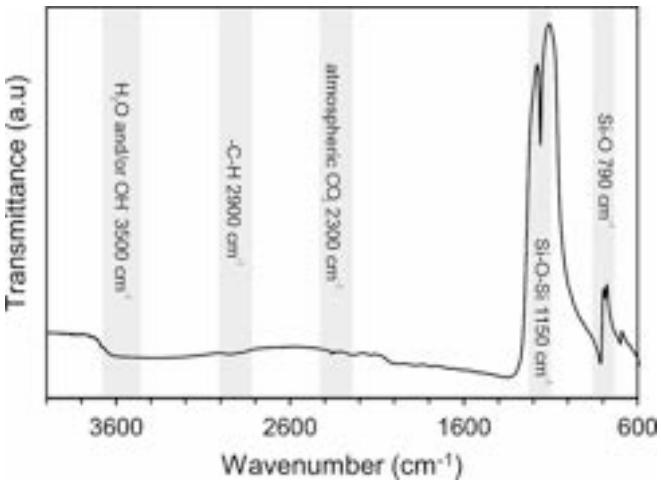

Fig. 9. FTIR spectrum collected on the amorphous silica associated with hectorite (see Fig. 8e for location of in-situ analysis). The FTIR spectrum shows the typical bands at of the Si-O and Si-O-Si vibrational modes around 790 and 50,500–900 cm^{-1}, respectively. The feature around 3500 cm^{-1} is due to the presence of structurally bonded H_2O and OH^-.

Limited coexistence of the 2200 nm and the 2306 nm features with low intensity absorption values is also in areas located outside the lithological boundaries of the volcano-sedimentary units, such as the SW margin of the caldera (Fig. 12b). This area is characterized by abundant scree deposits that comprise reworked material from the outcropping igneous units (i.e., biotite rhyolite, peralkaline rhyolite and McDermitt tuff; Henry et al., 2017) mixed with clay-bearing material redeposited after the erosion of the volcano-sedimentary units occurring at the top of the cliffs (see Appendix D). Hyperspectral and mineralogical analysis of the in-situ igneous units has confirmed a high spectral response around 2300 nm, due to the presence of primary biotite, and around 2200 nm in association with silicification features and presence of Al-clays (see Appendix D).

5.4. The High Rock caldera complex test

Mapping of the 2306 nm and 2200 nm features at the un-mineralized High Rock caldera complex yielded different results compared to those obtained for the McDermitt caldera (Fig. 14a, b). The 2306 and the 2200 nm bands locally show high values from the igneous country rocks, whilst a lack of spectral response can be observed for the volcano-clastic to sedimentary caldera-fill deposits. Localized high values of the feature at 2200 nm within caldera-fill units can be only observed in the marginal sector of the Virgin Valley caldera in association with dismissed opal

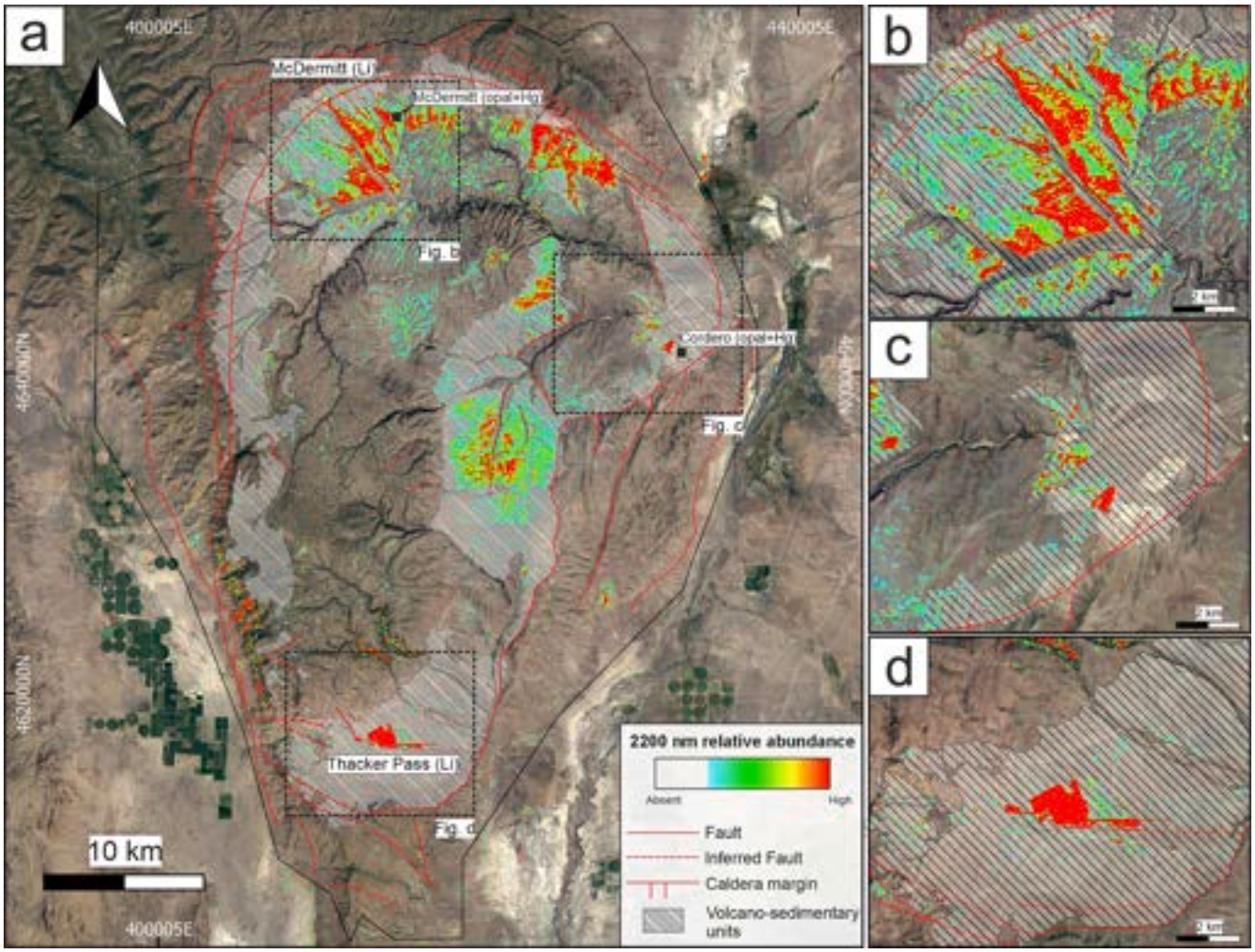

Fig. 10. a) Satellite maps of the band ratio values of the 2200 nm feature applied to the EnMap L2A scene of the McDermitt caldera; c) to d) magnified mineral maps of the band ratio values of the 2200 nm feature in the McDermitt Li deposits, in the Cordero opal mine and in the Thacker Pass Li deposit. Coordinate reference system of satellite maps: WGS84/UTM zone 11N.

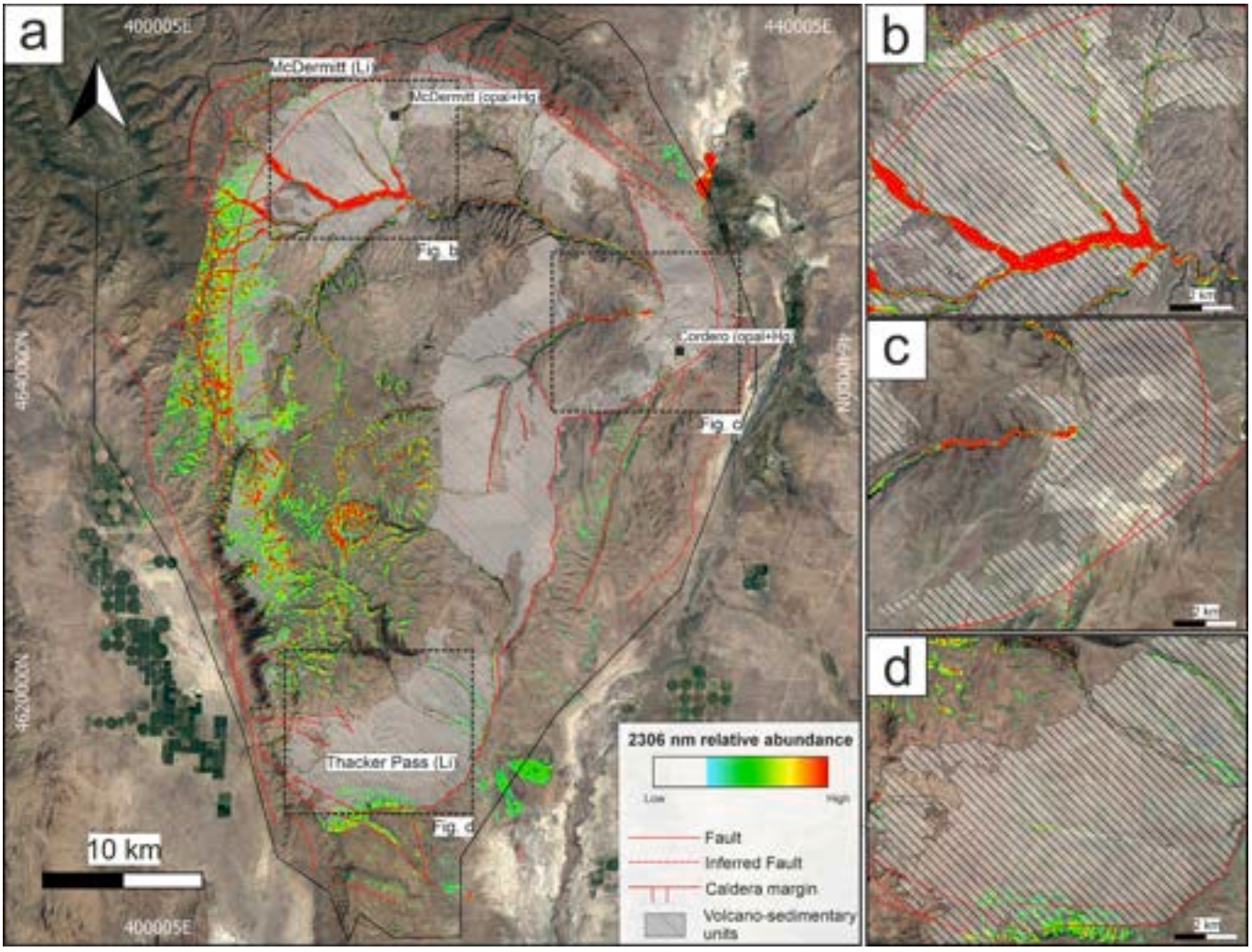

Fig. 11. a) Satellite maps of the band ratio values of the 2306 nm feature applied to the EnMap L2A scene of the McDermitt caldera; c) to d) magnified mineral maps of the band ratio values of the 2306 nm feature in the McDermitt Li deposits, in the Cordero opal mine and in the Thacker Pass Li deposit. Coordinate reference system of satellite maps: WGS84/UTM zone 11N.

mines (Zielinski, 1982). Furthermore, as opposed to the McDermitt caldera, no spatial coexistence of the features at 2306 and 2200 nm has been detected in the potentially Li-prospective volcano-sedimentary units.

6. Discussion

The sample- and satellite-based hyperspectral characterization of the McDermitt caldera presented in this study provides insights for improving or supporting local- to regional-scale exploration for Li mineralization in volcano-sedimentary environments. Analyses conducted on ground samples played an important role in validating and supporting the interpretation of satellite data, underscoring the importance of combining these two approaches. Employing the spectral range 400–2500 nm enabled to capture key spectral features, which were successfully employed for the identification and analysis of amorphous silica, zeolites, calcite, and various clay minerals such as hectorite and Fe-smectite. Despite the differences in spatial resolution between laboratory and satellite datasets, the adopted methodology allowed the generation of maps of mineral distribution and spectral data on a regional scale.

6.1. Interpretation of proximal hyperspectral data

Hyperspectral analysis of representative ground samples collected from the Jindalee McDermitt Li deposit, complemented by conventional mineralogical and geochemical techniques (i.e., XRD, SEM-EDS, automated SEM, EPMA, FTIR and bulk-rock geochemistry), allowed the identification of the main ore and alteration assemblages and their textural relationships. This multi-technique approach revealed three main assemblages:

1. *Silica + Fe-smectite(±hectorite):* this assemblage was predominantly observed in the shallow lithologies that despite are affected by an intense alteration have locally preserved hectorite, resulting in the development of surficial Li anomalies.
2. *Silica + hectorite(±zeolites):* this assemblage is characteristic of the Li-mineralized zones and associated siliceous lacustrine sediments, and largely originated during the ore-forming event linked to the alteration of volcanic glass-rich extrusive lithologies in a lacustrine environment.
3. *Zeolites + silica(±Fe-smectite):* this assemblage is typically associated with the zeolite facies, which marks horizons in the McDermitt orebody of intense alteration of pyroclastic units.

Our results point out that silica compounds, such as poorly

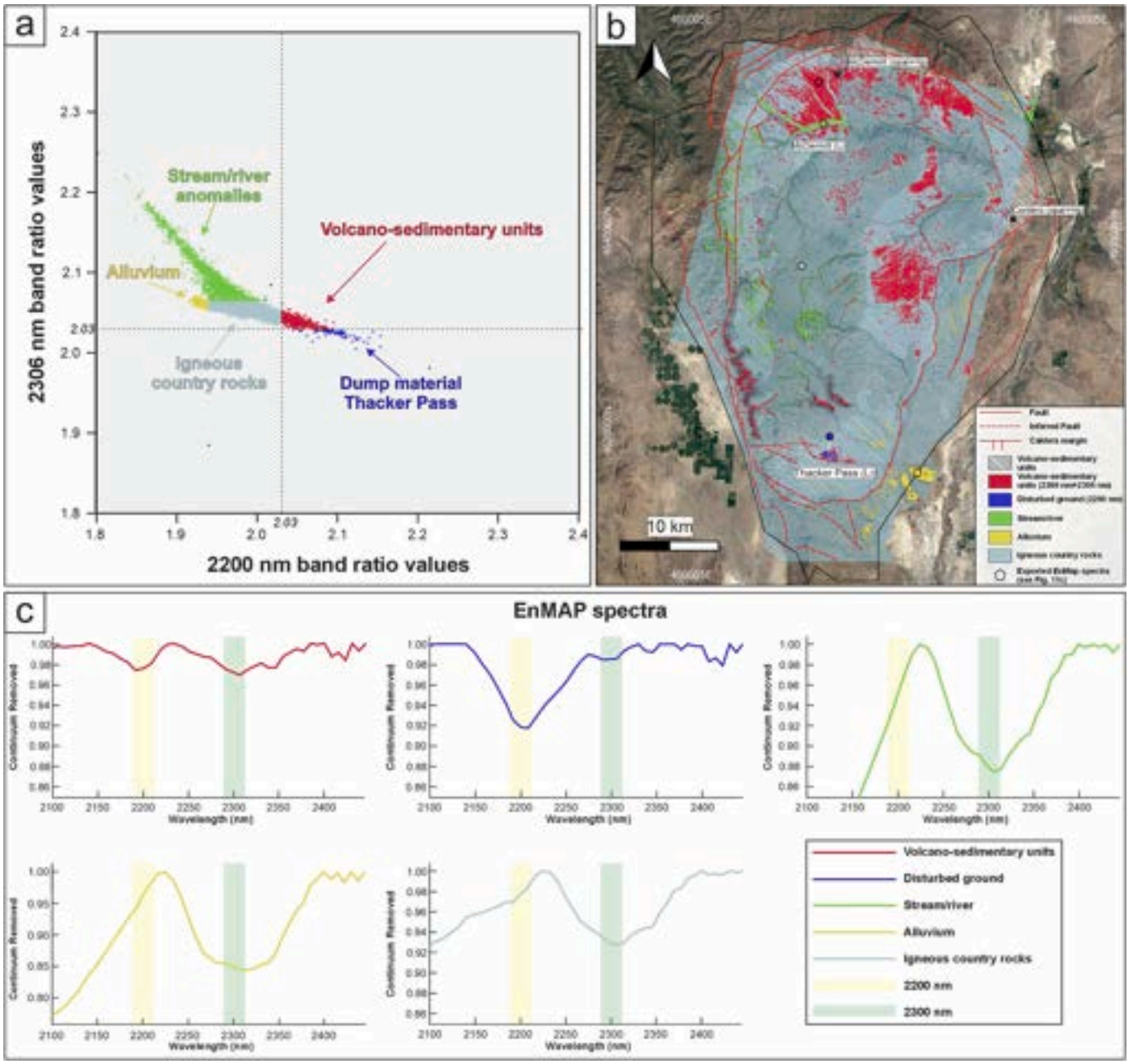

Fig. 12. a) Scatter plot of spectral band ratio values at 2200 nm against 2306 nm based on EnMap satellite data; b) satellite map displaying the spatial distribution of the clusters identified in the scatter plot; c) EnMAP reflectance spectra exported from representative localities of the clusters identified in Fig. 12a. Coordinate reference system of satellite maps: WGS84/UTM zone 11N.

crystalline diagenetic silica, are closely associated both with the mineralized horizons and with their shallow expressions (i.e., overburden units and sub-cropping hectorite-rich sediments). Hyperspectral analysis indicates that amorphous silica exhibits varying absorption features, typically observed within the wavelength range of 2196 nm to 2215 nm. This spectral shift is attributed to chemical variations within the amorphous silica, particularly due to the presence of Al and H_2O, as confirmed through EPMA. However, distinguishing between these variations in the SWIR range presents a challenge, as the presence of Al can lead to ambiguities. Specifically, the Al content could also suggest the occurrence of Al-smectite, which displays an Al-OH absorption feature near 2200 nm (Bishop et al., 2008; Laukamp et al., 2021). The correct interpretation of the hyperspectral data requires to differentiate between Al-related spectral signatures in silica and those of Al-bearing smectites. According to field and drillcore observation on the analyzed samples (Figs. 2, 5), the McDermitt orebody is covered by altered tuffaceous units showing a disseminated to spherulitic silica alteration. Furthermore, the XRD and FTIR studies support that silica compounds are locally amorphous and are characterized by a degree of hydration, in line with the overall characteristics observed for opal-A species that form in diagenetic systems (e.g., Hesse, 1989). This inference supports the hyperspectral analysis of the McDermitt samples, and that opal-like compounds can contribute to the development of the absorption feature at around 2200 nm. The effectiveness of the employed methodology to discern variations in chemical composition was documented in the analysis of smectites, particularly those containing the Fe-OH bond. This capability is demonstrated by the spectrum presented in Fig. 7h, which displays a distinct shift in the Fe-OH absorption feature, ranging from 2283 nm to 2292 nm that allows Fe-smectite and other smectite species to be distinguished. The successful identification of different smectite

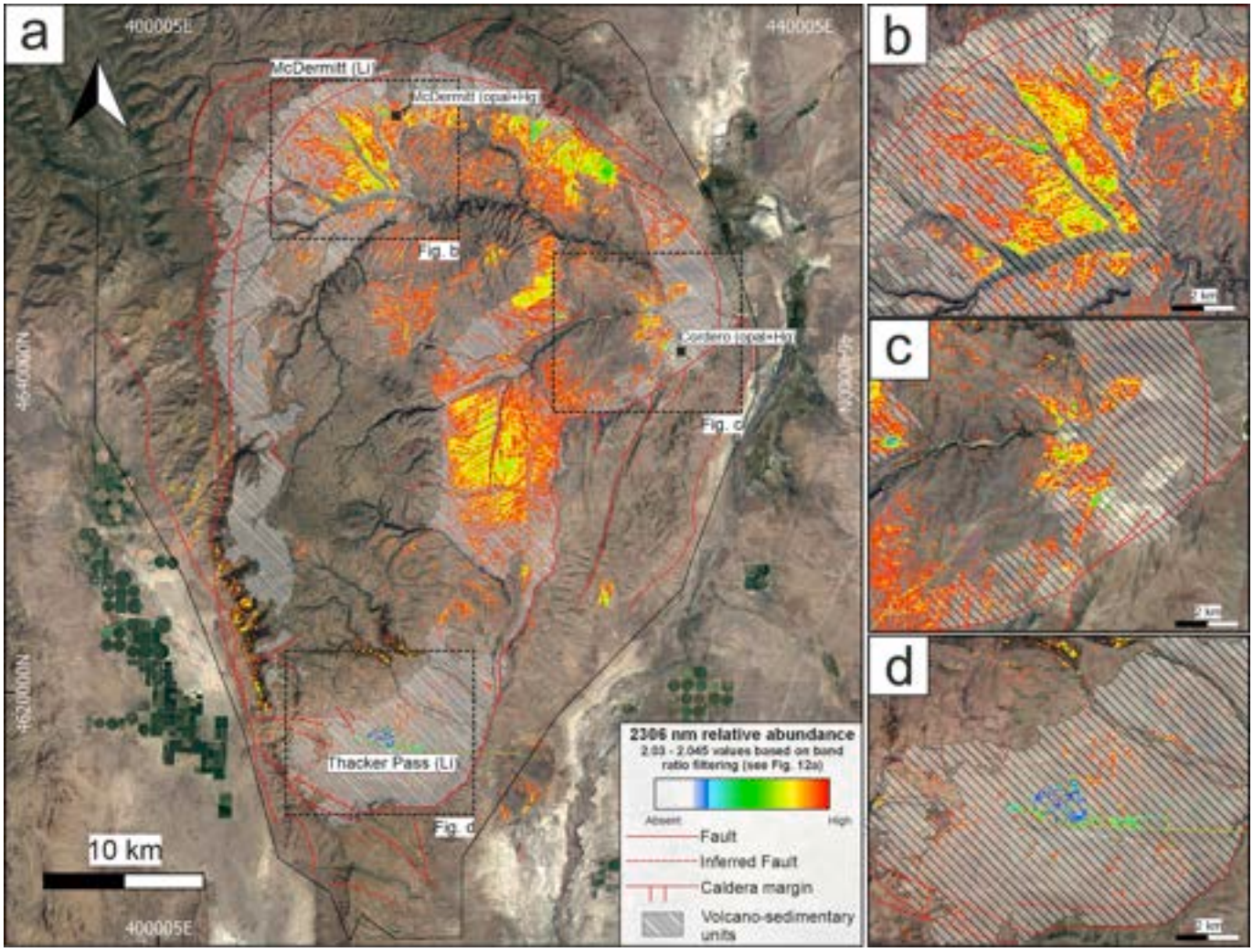

Fig. 13. a) Satellite maps of the 2306 band ratio in the 2.03–2.045 values cluster range, applied to the EnMap L2A scene of the McDermitt caldera; c) to d) magnified mineral maps of the 2306 band ratio in the 2.03–2.045 values cluster range in the McDermitt Li deposits, in the Cordero opal mine and in the Thacker Pass Li deposit. Coordinate reference system of satellite maps: WGS84/UTM zone 11N.

types is particularly relevant for targeting Li mineralization in volcano-sedimentary terranes, where Li is preferentially enriched in Mg-rich trioctahedral clays due to the presence of larger sites in their octahedra (e.g., Tardy et al., 1972). The distinction between different zeolite types was a more significant challenge. Zeolites display a key diagnostic absorption feature at around 2500 nm that is outside the spectral range of the instruments employed in this study (Cloutis et al., 2002; Kodikara et al., 2023). Consequently, the chemical classification of zeolites could not be achieved, thereby restricting the differentiation of these minerals based exclusively on the available spectra data.

6.2. *Interpretation of the alteration footprint related to McDermitt caldera through satellite imaging*

The laboratory-derived spectral characterization of samples from the Jindalee McDermitt Li deposit has enabled the use of EnMAP hyperspectral data to map alteration zones with high Li mineralization potential in the wider McDermitt caldera. The EnMAP data were useful to discriminate the 2200 nm and 2306 nm absorption features, corresponding to amorphous silica (opal-like) and hectorite, respectively. The satellite hyperspectral maps (Figs. 10–13) show a spatial correlation between amorphous silica and hectorite, confirming the mineral association revealed in mineralized samples, and displayed high abundances within the Li-prospective volcano-sedimentary units (mapped as "intracaldera sediments" and as "Quaternary units" by Henry et al., 2017), hence suggesting that this mineral assemblage serves as a reliable vector for identifying potential lithium mineralization sites. The coherence between satellite and laboratory data confirms the presence of these target minerals and validates the efficacy of satellite hyperspectral imaging in delineating mineralization vectors over large and lithologically complex areas. However, the identification of volcano-sedimentary lithium deposits through remote sensing techniques presents certain challenges, particularly arising from the spectral ambiguities that occur between hectorite and non-Li-bearing Mg-smectites (such as saponite), as well as micas, which can be respectively present in the secondary assemblages and in the associated igneous country rocks. Hectorite, a Li-rich Mg-smectite, is characterized by a diagnostic absorption feature at 2306 nm, attributed to the Mg-OH bending vibration, along with a secondary, weaker absorption at 2384 nm (Kokaly et al., 2017). Despite these distinctive features, the spectral signature of hectorite is not unique. Other minerals, such as sepiolite, saponite, amphiboles and magnesium carbonates (e.g., magnesite), exhibit primary absorption features near 2310 nm, complicating their distinction from hectorite (Bishop et al., 2008; Kokaly et al., 2017; Laukamp et al., 2021). This issue is further amplified when the secondary absorption at 2384 nm is either insufficiently robust to be discernible or obscured by preprocessing techniques designed to reduce the effects of noise in the data. To mitigate these challenges, the spatial association of amorphous

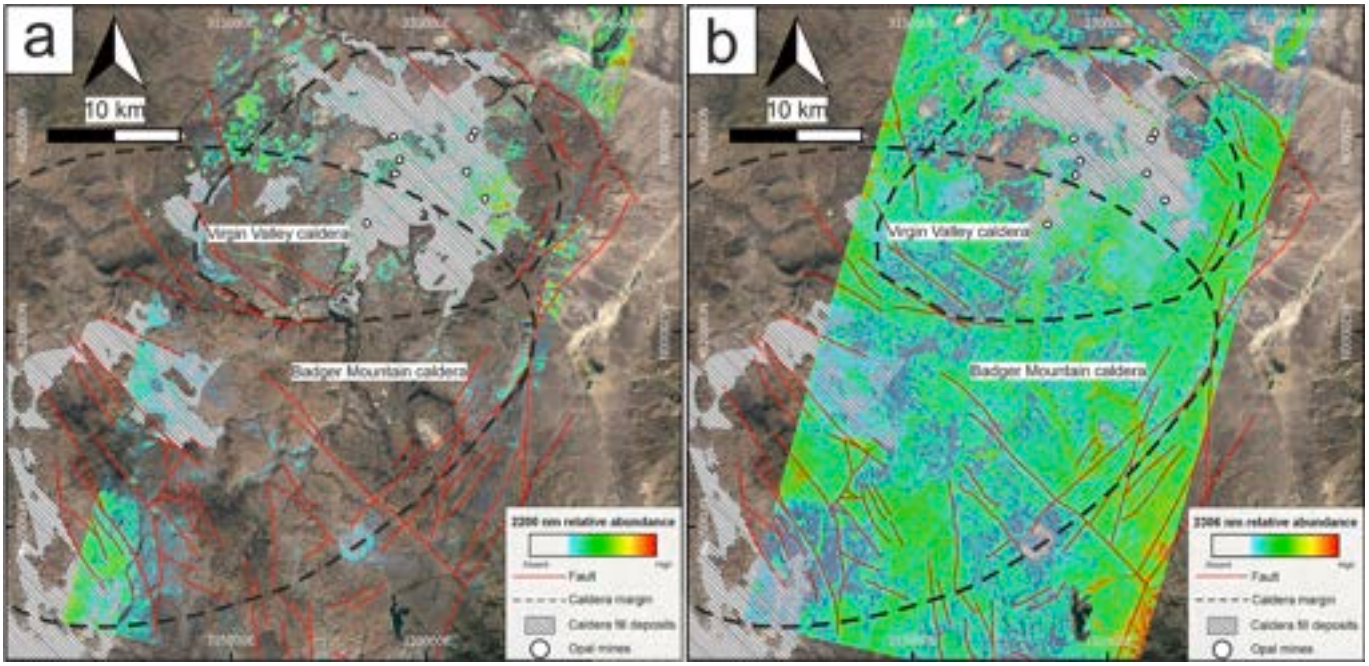

Fig. 14. Satellite maps of the target spectral features applied to the EnMap L2A scene of the High Rock caldera complex: a) map of the band ratio values of the 2200 nm feature; a) map of the band ratio values of the 2306 nm feature. Coordinate reference system of satellite maps: WGS84/UTM zone 11N.

silica with hectorite and its occurrence within volcano-sedimentary units has proven to be an effective discriminant to target Li mineralized bodies in the case of the McDermitt caldera. In this sense, the binary diagram showing the relationship between the absolute values of the 2200 nm and of the 2306 nm bands (Fig. 12a) allows the recognition of data clusters characterized by significant absorption features of both the indicated spectral bands, which correspond to Li-prospective volcano-sedimentary units (Fig. 12b-c; Fig. 13). Following the employed band ratio method, relevant spectral signatures only correspond to band ratios above 2. In our case, to target significant values of the feature at 2200 nm we have considered band ratios above the statistical threshold of 2.03. Within the areas that satisfied these criteria, we have selected data points where the values of the feature at 2200 nm were spatially correlated with a spectral response of the feature at 2306 nm (Fig. 12a). Band ratio values lower than the threshold were considered to map other lithological groupings occurring in the caldera. For example, igneous units and the stream sediments have high band ratio values of the 2306 nm feature but are not associated with 2200 values above the threshold, while the disturbed ground material at Thacker Pass displays high band ratio values of the feature at 2200 nm and very minor values of that at 2306 nm (Fig. 12b-c; Fig. 13). A few areas that are marked by the coexistence of both the 2200 nm and the 2306 nm band cannot be considered as potential Li-targets because they are highlighting barren lithologies, and thus indicating that the significance of this approach as exploration tool strictly depends on an adequate understanding of the ground geology.

6.3. *Implications for the exploration targeting of volcano-sedimentary lithium deposits*

Hyperspectral remote sensing presents a powerful tool for the rapid detection of mineralogical anomalies resulting from the mineralizing process for many styles of ore deposits. In the example of volcano-sedimentary Li deposits, potential ore bearing units are characterized by specific mineral assemblages, which include Li-containing Mg-smectites and silica occurring within stratiform sequences that may be significant in their spatial extent. This mineralogical signature is a consequence of specific diagenetic conditions and minerogenic pathways that promotes the enrichment and retention of lithium. Specifically, previous studies have demonstrated that the Li mineralization in volcano-sedimentary deposits mostly originate from the alteration of Li-fertile, highly fractionated, and glass-rich tuffaceous rocks within short-lived endorheic lacustrine systems developed in volcanic terranes (e.g., Benson et al., 2023; Castor and Henry, 2020; Putzolu et al., 2025). In such settings, circulation of fluids with high pH and high silica activity leads to alteration of the host igneous units, and subsequent segregation of poorly crystalline silica from the SiO_2 excess linked to the glass-to-hectorite transformation (Putzolu et al., 2025). In the framework of the Minerals System Approach (MSA) of McCuaig et al. (2010), the latter conditions are defined as *Constituent Process*, namely a process that is essential for the formation of the *Mineralogical Trap* that constitute volcano-sedimentary Li deposits (Armstrong et al., 2024; Putzolu et al., 2025). However, this Constituent Process is one of several interdependent processes that must occur within the geological environments where volcano-sedimentary Li mineralization are originated. The five Constituent Processes and the resultant Critical Processes are as follows (Fig. 15):

1. *Source:* Li-fertile felsic magmas associated with melting of clay-rich metasedimentary sources.
2. *Pathway:* regional- to local-scale extensional structures allowing the migration of Li-rich melts from the middle to the upper crust and eruption of volcanic glass-rich pyroclastic rocks.
3. *Physical trap:* endorheic lacustrine basins, such as nested-caldera and rift basins, which act as final repositories for the deposition of fertile pyroclastic rocks and restrict Li loss through fluid outflow.
4. *Mineralogical trap:* development of alkaline diagenetic conditions and formation of Li-bearing assemblages stable under high pH and saline environments.
5. *Preservation:* tectonic and climatic stability accounting for the persistence of the environmental and physiochemical conditions favorable for the preservation of the Li mineral trap.

Considering the MSA framework, each Constituent Process can be associated with *Targeting Elements*, which represent their geological expressions (McCuaig et al., 2010). In the case of volcano-sedimentary Li

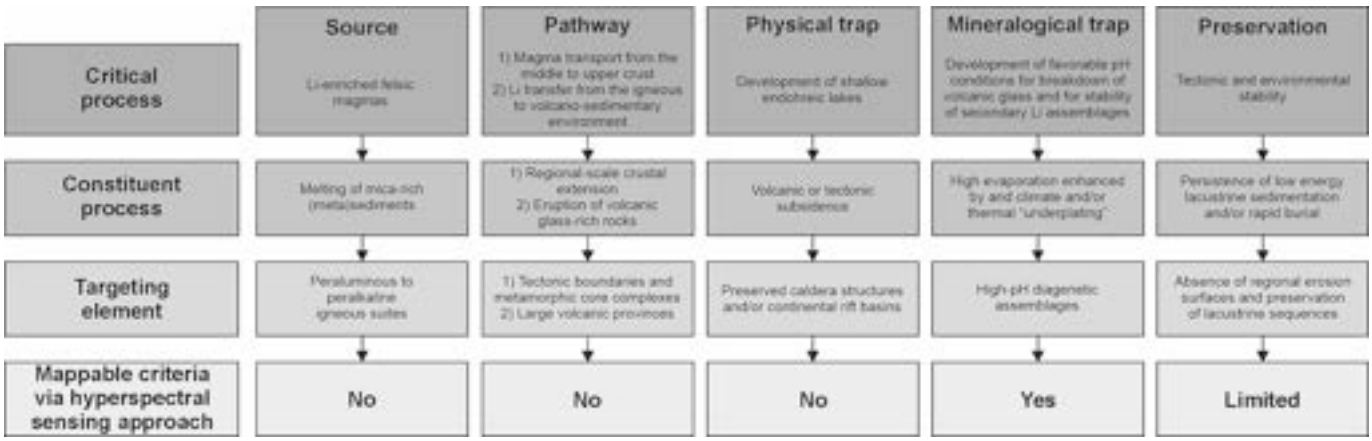

Fig. 15. Mineral system approach (MSA) applied to volcano-sedimentary Li deposits, with reference to the potential of hyperspectral sensing to target mappable criteria related to the development and preservation of suitable mineralogical traps (see section 6.3 for details).

deposits, the resultant Targeting Elements of the Mineralogical and Physical Traps are the specific ore mineralogy, and geological evidence of a closed lacustrine environment of deposition. The features of volcano-sedimentary Li mineralization cannot be easily identified by geologists on the ground as they generally include very fine-grained material, and lithium remains a challenging element to measure directly by portable elemental analyzers.

Our hyperspectral study of the Li mineralization in the McDermitt caldera has successfully detected spectral features of the hectorite+silica ore assemblage (Fig. 6). The EnMap satellite mapping has confirmed that the volcano-sedimentary units exert a strong lithological control for the 2200 + 2306 nm spectral bands, which show a high abundance within the Jindalee McDermitt tenure (Figs. 10 and 13), and also in other areas of the caldera (i.e., NNE and E sectors) that were shown to be prospective for similar shallow Li-smectite mineralization by recent exploration surveys (Chariot Corp. Ltd, 2023). The reliability of this approach was assessed by satellite mapping of the 2306 and 2200 nm features at the High Rock caldera complex, which is a silicic volcanic center that share several critical features with the McDermitt caldera (e.g., abundance of highly fractionated peralkaline rhyolites and episodes of lacustrine sedimentation; Coble and Mahood, 2016), yet this system did not develop suitable mineralogical traps for volcano-sedimentary Li mineralization. The test on the unmineralized High Rock caldera complex confirms a lack of the 2200 + 2306 nm bands association (Fig. 14a, b). This result confirms the specificity of this spectral footprint and supports the potential of the proposed approach to identify the presence of the key minerals characteristic of the Mineralogical Trap, thus providing a *Mappable Criteria* or proxy to be used as exploration tool (Fig. 15). However, there are three key caveats to the application of this strategy:

1. *Detection of a single Constituent Process*: this methodology is focused on the detection of the presence and spatial extent of potential Mineralogical Traps. It does not provide any insights into the other Constituent Processes, such as the initial source of Li nor the pathway by which Li is transported from the source to Mineralogical Trap. Therefore, although a suitable Mineralogical Trap is identifiable through this methodology, the lithium fertility of the targeted system will need to be defined through conventional mineralogical-geochemical analysis of ground samples.
2. *False Positive Mineralogy:* the 2306 nm and 2200 nm features used to discriminate the presence of the hectorite+silica assemblage are not unique to these minerals and are also typical absorption bands of biotite, white micas, Al-clays and non-Li-bearing Mg-smectites (e.g., saponite) resulting from the vibrational response of the Al-OH and Mg-OH groups (e.g., Laukamp et al., 2021; Meyer et al., 2022). Primary micas are common rock-forming minerals in the igneous suites associated with volcano-sedimentary Li deposits (Putzolu et al., 2025), and hence can affect the effective satellite mapping of the Li-prospective lacustrine deposits and lead to false positives. An example of this challenge is also highlighted by the outcomes obtained for the McDermitt caldera, which locally resulted in anomalous spectral responses of the 2306 nm and 2200 nm features in areas characterized by outcrops of intensively silicified biotite-rich igneous lithologies (Appendix D). Therefore, any attempt at mapping the 2306 nm and 2200 nm features should be informed by a detailed geological and satellite-based morphostructural analysis of the study area aimed at outlining structural features, such as caldera walls or extensional faults, which potentially mark the transition from the igneous country rocks to the Li-prospective volcano-sedimentary sequences. Furthermore, to differentiate between micas and different smectite species, it is useful to consider the second absorption feature of hectorite at around 2380 nm, which can be also used to distinguish between hectorite and non-Li-smectites (Laukamp et al., 2021 and references therein). Alternatively, the adoption of an imaging system in the TIR (Thermal Infrared) range can give further clues to differentiate the volcano-sedimentary units from the igneous country rocks. Specifically, TIR imaging (e.g., ASTER TIR) has a demonstrated capability to delineate lithologies with high abundances of non-hydrated silica phases such as quartz (Rockwell and Hofstra, 2008; Goryniuk et al., 2004), which is dominant in the igneous assemblages of extrusive felsic lithologies (i.e., rhyolites) associated with volcano-sedimentary Li deposits (e.g., Benson et al., 2017a, 2017b; Henry et al., 2017).
3. *Exposure:* volcano-sedimentary Li deposits largely consist of shallow mineralization, and hence can be easily targeted by remote sensing approaches when exposed at surface. However, in some mineral districts post-mineralization tectonic and/or volcanic processes can affect the level of exposure and hence the effectiveness of remote sensing methods. For example, volcano-sedimentary Li deposits from the Western Balkan Li—B metallogenic zone experienced burial following episodes of gravitational collapse that led to tectonic subsidence (Borojević Šoštarić and Brenko, 2022), while, in other instances (e.g., Thacker Pass Li deposit, USA; Benson et al., 2023; Castor and Henry, 2020) late volcanic processes can seal the volcano-sedimentary Li sequence via emplacement of lava flow units.

7. Conclusions

This study has demonstrated the effectiveness of integrating proximal hyperspectral imaging with satellite remote sensing to delineate

mineralogical assemblages and identify potential lithium mineralization zones within the volcano-sedimentary units of the McDermitt caldera (USA). The hyperspectral data obtained from samples, validated through mineralogical and geochemical analyses, underlined a close association between Mg(Li)-smectite (hectorite) and amorphous silica, providing a reliable indicator of Li mineralization in a volcano-sedimentary environment. The EnMAP satellite maps reveal a significant spatial correlation between the target mineral features within the caldera, enhancing the potential to pinpoint lithium-bearing units on a regional scale. This validates the effectiveness of hyperspectral remote sensing for mineral exploration and provides a valuable tool for the targeting of geological environments with analogous mineralogical traps observed for volcano-sedimentary Li mineralization. The test conducted on the nearby and unmineralized High Rock caldera complex (USA) further supported the specificity of the hectorite-amorphous silica spectral association as a potential hyperspectral-mineralogical vector for Li deposits in volcano-sedimentary environments. Nonetheless, the spectral ambiguities presented by Mg-smectites, micas, and other minerals emphasize the necessity of integrating spectral data with mineralogical and geological information to improve precision in mineral targeting.

CRediT authorship contribution statement

F. Corrado: Writing – review & editing, Writing – original draft, Visualization, Validation, Software, Methodology, Investigation, Formal analysis, Data curation, Conceptualization. **F. Putzolu:** Writing – review & editing, Writing – original draft, Visualization, Validation, Supervision, Software, Project administration, Methodology, Investigation, Funding acquisition, Formal analysis, Data curation, Conceptualization. **R.N. Armstrong:** Writing – review & editing, Validation, Funding acquisition. **N. Mondillo:** Writing – review & editing, Validation, Supervision, Conceptualization. **R. Chirico:** Writing – review & editing, Formal analysis, Conceptualization. **B. Casarotto:** Resources, Methodology. **M. Massironi:** Resources, Methodology. **D. Fuller:** Methodology. **R. Ball:** Writing – review & editing, Funding acquisition. **R.J. Herrington:** Writing – review & editing, Validation, Funding acquisition.

Declaration of competing interest

The authors declare that they have no known competing financial interests that could have appeared to influence the work reported in this paper.

Data availability

Data will be made available on request.

Acknowledgments

This study has received funding from the NERC Lithium for Future Technology LiFT (ID: NE/V007068/1) project and from Jindalee Lithium Ltd. This research is also part of the ongoing PhD project of F. Corrado at the University of Naples “Federico II” (Italy), under the supervision of N. Mondillo. The authors wish to thank the personnel of the Image and Analysis Centre (Natural History Museum, London), especially Alejandro Cortes Calderon, Wren Montgomery, Jens Najorka, Cindy Broderick and Tobias Salge, for the assistance during the analytical work, and Jindalee Lithium Ltd. for granting access to the McDermitt deposit and for geological discussions. We are also grateful to the Associate Editor Yong Wang and to the Editor in Chief Jing. M. Chen for the editorial handling and to the three anonymous reviewers for their careful revision which greatly enhanced the quality of the paper.

Appendix A. Supplementary data

Supplementary data to this article can be found online at https://doi.org/10.1016/j.rse.2025.114724.

References

Adamo, I., Ghisoli, C., Caucia, F., 2010. A contribution to the study of FTIR spectra of opals. Neu Jb. Mineral. Abh. 187, 63–68. https://doi.org/10.1127/0077-7757/2010/0161.

Armstrong, R.N., Putzolu, F., Benson, T., Herrington, R.J., 2024. A minerals systems approach for li-volcano-sedimentary deposits. In: Society of Economic Geologists (SEG) Annual Meeting 2024, Windhoek, Namibia. https://www.segweb.org/SEG/Events/SEG-Conference-Archive/SEG/Events/SEG-Conference-Archive.aspx.

Asadzadeh, S., Zhou, X., Chabrillat, S., 2024. Assessment of the spaceborne EnMAP hyperspectral data for alteration mineral mapping: a case study of the Reko Diq porphyry CuAu deposit, Pakistan. Remote Sens. Environ. 314, 114389. https://doi.org/10.1016/j.rse.2024.114389.

Benson, T.R., Coble, M.A., Rytuba, J.J., Mahood, G.A., 2017a. Lithium enrichment in intracontinental rhyolite magmas leads to li deposits in caldera basins. Nat. Commun. 8, 270. https://doi.org/10.1038/s41467-017-00234-y.

Benson, T.R., Mahood, G.A., Grove, M., 2017b. Geology and 40Ar/39Ar geochronology of the middle Miocene McDermitt volcanic field, Oregon and Nevada: silicic volcanism associated with propagating flood basalt dikes at initiation of the Yellowstone hotspot. Geol. Soc. Am. Bull. 129, 1027–1051. https://doi.org/10.1130/B31642.1.

Benson, T.R., Coble, M.A., Dilles, J.H., 2023. Hydrothermal enrichment of lithium in intracaldera illite-bearing claystones. Sci. Adv. 9, eadh8183. https://doi.org/10.1126/sciadv.adh8183.

Bishop, J.L., Lane, M.D., Dyar, M.D., Brown, A.J., 2008. Reflectance and emission spectroscopy study of four groups of phyllosilicates: smectites, kaolinite-serpentines, chlorites and micas. Clay Miner. 43, 35–54. https://doi.org/10.1180/claymin.2008.043.1.03.

Booysen, R., Lorenz, S., Thiele, S.T., Fuchsloch, W.C., Marais, T., Nex, P.A., Gloaguen, R., 2022. Accurate hyperspectral imaging of mineralised outcrops: an example from lithium-bearing pegmatites at Uis, Namibia. Remote Sens. Environ. 269, 112790. https://doi.org/10.1016/j.rse.2021.112790.

Borojević Šoštarić, S., Brenko, T., 2022. The Miocene Western Balkan lithium-boron metallogenic zone. Miner. Depos. 58, 639–658. https://doi.org/10.1007/s00126-022-01151-x.

Bowell, R.J., Lagos, L., de los Hoyos, C.R., Declercq, J., 2020. Classification and characteristics of natural lithium resources. Elements 16, 259–264. https://doi.org/10.2138/gselements.16.4.259.

Calvin, W.M., Pace, E.L., 2016. Mapping alteration in geothermal drill core using a field portable spectroradiometer. Geothermics 61, 12–23. https://doi.org/10.1016/j.geothermics.2016.01.005.

Cardoso-Fernandes, J., Teodoro, A.C., Lima, A., Perrotta, M., Roda-Robles, E., 2020. Detecting Lithium (li) mineralizations from space: current research and future perspectives. Appl. Sci. 10, 1785. https://doi.org/10.3390/app10051785.

Castor, S.B., Henry, C.D., 2000. Geology, geochemistry, and origin of volcanic rock-hosted uranium deposits in northwestern Nevada and southeastern Oregon, USA. Ore Geol. Rev. 16, 1–40. https://doi.org/10.1016/S0169-1368(99)00021-9.

Castor, S.B., Henry, C.D., 2020. Lithium-rich claystone in the McDermitt caldera, Nevada, USA: geologic, mineralogical, and geochemical characteristics and possible origin. Minerals 10, 68. https://doi.org/10.3390/min10010068.

Chabrillat, S., Foerster, S., Segl, K., Beamish, A., Brell, M., Asadzadeh, S., Milewski, R., Ward, K.J., Brosinsky, A., Koch, K., Scheffler, D., 2024. The EnMAP spaceborne imaging spectroscopy mission: initial scientific results two years after launch. Remote Sens. Environ., 114379 https://doi.org/10.1016/j.rse.2024.114379.

Chariot Corp. Ltd, 2023. Annual Report 2023. https://www.chariotcorporation.com/pdf/bf3fb309-bae6-4658-b284-51a1fd2b35e3/Annual-Report-2023.pdf.

Chauviré, B., Pineau, M., Quirico, E., Beck, P., 2021. Near infrared signature of opaline silica at Mars-relevant pressure and temperature. Earth Planet. Sci. Lett. 576, 117239. https://doi.org/10.1016/j.epsl.2021.117239.

Clark, R.N., King, T.V.V., Klejwa, M., Swayze, G.A., Vergo, N., 1990. High spectral resolution reflectance spectroscopy of minerals. J. Geophys. Res. 95, 12653–12680. https://doi.org/10.1029/JB095iB08p12653.

Cloutis, E.A., Asher, P.M., Mertzman, S.A., 2002. Spectral reflectance properties of zeolites and remote sensing implications. J. Geophys. Res. 107. https://doi.org/10.1029/2000JE001467.

Coble, M.A., Mahood, G.A., 2012. Initial impingement of the Yellowstone plume located by widespread silicic volcanism contemporaneous with Columbia River flood basalts. Geology 40, 655–658. https://doi.org/10.1130/G32692.1.

Coble, M.A., Mahood, G.A., 2016. Geology of the High Rock caldera complex, northwest Nevada, and implications for intense rhyolitic volcanism associated with flood basalt magmatism and the initiation of the Snake River Plain–Yellowstone trend. Geosphere 12, 58–113. https://doi.org/10.1130/GES01162.1.

Cudahy, T., Jones, M., Thomas, M., Laukamp, C., Caccetta, M., Hewson, R., Rodger, A., Verrall, M., 2008. Next Generation Mineral Mapping: Queensland Airborne HyMap and Satellite ASTER Surveys 2006–2008. https://doi.org/10.13140/RG.2.1.2828.1844.

Gaffey, S.J., 1986. Spectral reflectance of carbonate minerals in the visible and near infrared (0.35-2.55 microns); calcite, aragonite, and dolomite. Am. Mineral. 71, 151–162.

Goryniuk, M.C., Rivard, B.A., Jones, B., 2004. The reflectance spectra of opal-a (0.5–25 μm) from the Taupo volcanic zone: spectra that may identify hydrothermal systems on planetary surfaces. Geophys. Res. Lett. 31, 2004GL021481. https://doi.org/10.1029/2004GL021481.

Green, A.A., Berman, M., Switzer, P., Craig, M.D., 1988. A transformation for ordering multispectral data in terms of image quality with implications for noise removal. IEEE Trans. Geosci. Remote Sensing 26, 65–74. https://doi.org/10.1109/36.3001.

Henry, C.D., Castor, S.B., Starkel, W.A., Ellis, B.S., Wolff, J.A., Laravie, J.A., McIntosh, W. C., Heizler, M.T., 2017. Geology and evolution of the McDermitt caldera, northern Nevada and southeastern Oregon, western USA. Geosphere 13, 1066–1112. https://doi.org/10.1130/GES01454.1.

Hesse, R., 1989. Silica diagenesis: origin of inorganic and replacement cherts. Earth-Sci. Rev. 26 (1-3), 253–284. https://doi.org/10.1016/0012-8252(89)90024-X.

Jiang, Q., Dai, J., Wang, D., Wang, C., Tian, S., 2023. Lithium-bearing pegmatite exploration in Western Altun, Xinjiang, using remote-sensing technology. Acta Geol. Sin. 97, 681–694. https://doi.org/10.1111/1755-6724.15025.

Kirsch, M., Mavroudi, M., Thiele, S., Lorenz, S., Tusa, L., Booysen, R., Herrmann, E., Fatihi, A., Möckel, R., Dittrich, T., Gloaguen, R., 2023. Underground hyperspectral outcrop scanning for automated mine-face mapping: the lithium deposit of Zinnwald/Cínovec. Photogramm. Rec. 38, 408–429. https://doi.org/10.1111/phor.12457.

Kodikara, G.R.L., McHenry, L.J., Van Der Meer, F.D., 2023. Spectral mapping of zeolite bearing paleolake deposits at Lake Tecopa, California and its implications for mapping zeolites on Mars. GeoGeo 2, 100119. https://doi.org/10.1016/j.geogeo.2022.100119.

Kokaly, R.F., Clark, R.N., Swayze, G.A., Livo, K.E., Hoefen, T.M., Pearson, N.C., Wise, R. A., 2017. Data series. Data series. US Geological Survey, Reston, VA. https://doi.org/10.3133/ds1035.

Kumar, C., Chatterjee, S., Oommen, T., Guha, A., 2020. Automated lithological mapping by integrating spectral enhancement techniques and machine learning algorithms using AVIRIS-NG hyperspectral data in gold-bearing granite-greenstone rocks in Hutti, India. Int. J. Appl. Earth Obs. 86, 102006. https://doi.org/10.1016/j.jag.2019.102006.

Laukamp, C., 2022. Geological mapping using mineral absorption feature-guided band-ratios applied to prisma satellite hyperspectral level 2D imagery. In: IGARSS 2022–2022 IEEE International Geoscience and Remote Sensing Symposium. Presented at the IGARSS 2022–2022 IEEE International Geoscience and Remote Sensing Symposium. IEEE, Kuala Lumpur, Malaysia, pp. 5981–5984. https://doi.org/10.1109/IGARSS46834.2022.9884015.

Laukamp, C., Rodger, A., LeGras, M., Lampinen, H., Lau, I.C., Pejcic, B., Stromberg, J., Francis, N., Ramanaidou, E., 2021. Mineral Physicochemistry underlying feature-based extraction of mineral abundance and composition from shortwave, mid and thermal infrared reflectance spectra. Minerals 11, 347. https://doi.org/10.3390/min11040347.

de Los Reyes, R., Langheinrich, M., Schwind, P., Richter, R., Pflug, B., Bachmann, M., Müller, R., Carmona, E., Zekoll, V., Reinartz, P., 2020. PACO: Python-based atmospheric correction. Sensors 20, 1428. https://doi.org/10.3390/s20051428.

McCuaig, T.C., Beresford, S., Hronsky, J., 2010. Translating the mineral systems approach into an effective exploration targeting system. Ore Geol. Rev. 38, 128–138. https://doi.org/10.1016/j.oregeorev.2010.05.008.

Meyer, J.M., Kokaly, R.F., Holley, E., 2022. Hyperspectral remote sensing of white mica: a review of imaging and point-based spectrometer studies for mineral resources, with spectrometer design considerations. Remote Sens. Environ. 275, 113000. https://doi.org/10.1016/j.rse.2022.113000.

Meyer, J.M., Swayze, G.A., Kokaly, R.F., Stillings, L.L., Benzel, W.M., Hoefen, T.M., Cox, E., 2023. Mapping lithium bearing hectorite clay using imaging spectroscopy. In: IGARSS 2023-2023 IEEE International Geoscience and Remote Sensing Symposium, pp. 3708–3709. https://doi.org/10.1109/IGARSS52108.2023.10282680.

Putzolu, F., Armstrong, R.N., Ball, R., Meyer, P., Herrington, R.J., 2023. The McDermitt deposit (Oregon, US): Preliminary results from a li-clay volcano-sedimentary system. In: Society of Economic Geologists (SEG) Annual Meeting 2023, London, UK. https://www.segweb.org/SEG/Events/SEG-Conference-Archive/SEG/Events/SEG-Conference-Archive.aspx.

Putzolu, F., Armstrong, R.N., Benson, T.R., Boutt, D.F., Butler, K.L., Dolgopolova, A., Herrington, R.J., Ibarra, D.E., Munk, L.A., 2025. Volcano-sedimentary deposits: overview of an emergent type of Lithium resource. Econ. Geol. https://doi.org/10.5382/econgeo.5135.

Rockwell, B.W., Hofstra, A.H., 2008. Identification of quartz and carbonate minerals across northern Nevada using ASTER thermal infrared emissivity data—implications for geologic mapping and mineral resource investigations in well-studied and frontier areas. Geosphere 4, 218–246. https://doi.org/10.1130/GES00126.1.

Sorrentino, A., Chirico, R., Corrado, F., Laukamp, C., Di Martire, D., Mondillo, N., 2024. The application of PRISMA hyperspectral satellite imagery in the delineation of distinct hydrothermal alteration zones in the Chilean Andes: the Marimaca IOCG and the Río Blanco-Los Bronces cu-Mo porphyry districts. Ore Geol. Rev. 167, 105998. https://doi.org/10.1016/j.oregeorev.2024.105998.

Tardy, Y., Krempp, G., Trauth, N., 1972. Le lithium dans les minéraux argileux des sédiments et des sols. Geoch. Cosm. Act. 36, 397–412. https://doi.org/10.1016/0016-7037(72)90031-2.

Thiele, S.T., Lorenz, S., Kirsch, M., Acosta, I.C.C., Tusa, L., Herrmann, E., Möckel, R., Gloaguen, R., 2021. Multi-scale, multi-sensor data integration for automated 3-D geological mapping. Ore Geol. Rev. 136, 104252. https://doi.org/10.1016/j.oregeorev.2021.104252.

Zielinski, R.A., 1982. Uraniferous opal, Virgin Valley, Nevada: conditions of formation and implications for uranium exploration. J. Geochem. Explor. 16, 197–216. https://doi.org/10.1016/0375-6742(82)90010-3.